

HEAVY ATOM EFFECT ON INTERSYSTEM CROSSING OF A BORON  
DIFLUORIDE FORMAZANATE COMPLEX-BASED PHOTSENSITIZER



TUNYAWAT KHROOTKAEW

A Thesis Submitted in Partial Fulfillment of the Requirements for the  
Degree of Master of Science in Chemistry  
Suranaree University of Technology  
Academic Year 2024

ผลของอะตอมหนักต่อการข้ามสถานะพลังงานของสารประกอบเชิงซ้อนไวแสง  
โบรอนไดฟลูออไรด์ฟอร์มามาซาเน็ต

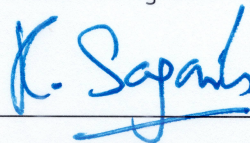


วิทยานิพนธ์นี้เป็นส่วนหนึ่งของการศึกษาตามหลักสูตรปริญญาวิทยาศาสตรมหาบัณฑิต  
สาขาวิชาเคมี  
มหาวิทยาลัยเทคโนโลยีสุรนารี  
ปีการศึกษา 2567

HEAVY ATOM EFFECT ON INTERSYSTEM CROSSING OF A BORON  
DIFLUORIDE FORMAZANATE COMPLEX-BASED PHOTSENSITIZER

Suranaree University of Technology has approved this thesis submitted in partial fulfillment of the requirements for the Degree of Master of Science.

Thesis Examining Committee



(Prof. em. Dr. Kritsana Sagarik)

Chairperson



(Assoc. Prof. Dr. Anyanee Kamkaew)

Member (Thesis Advisor)



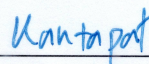
(Assoc. Prof. Dr. Suwit Suthirakun)

Member



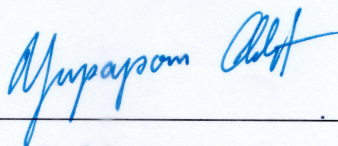
(Asst. Prof. Dr. Piyanut Pinyou)

Member



(Dr. Kantapat Chansaenpak)

Member



(Assoc. Prof. Dr. Yupaporn Ruksakulpiwat)

Vice Rector for Academic Affairs  
and Quality Assurance



(Prof. Dr. Santi Maensiri)

Dean of Institute of Science

ตุลยวัต ครูทแก้ว : ผลของอะตอมหนักต่อการข้ามสถานะพลังงานของสารประกอบเชิงซ้อนไวแสงโบรอนไดฟลูออไรด์ฟอร์มามาซาเนต (Heavy Atom Effect on Intersystem Crossing of a Boron Difluoride Formazanate Complex-Based Photosensitizer) อาจารย์ที่ปรึกษา : รองศาสตราจารย์ ดร.อัญญาณี คำแก้ว, 70 หน้า

คำสำคัญ: การรักษามะเร็งผ่านการกระตุ้นด้วยแสง, สารประกอบเชิงซ้อนโบรอนไดฟลูออไรด์ฟอร์มามาซาเนต, ผลกระทบอะตอมหนัก, การสร้างออกซิเจนเชิงเดี่ยว, TD-DFT

วิธีการรักษามะเร็งด้วยกระบวนการเหนี่ยวนำให้สารไวแสงผลิตสารที่เป็นพิษต่อเซลล์มะเร็งเป็นวิธีรักษาโดยใช้สารเคมีที่ตอบสนองต่อแสง ซึ่งจะเกี่ยวข้องกับการใช้แสงในการกระตุ้นสารที่ตอบสนองต่อแสงที่ได้รับ การรักษาด้วยวิธีนี้เป็นหนึ่งในทางเลือกสำหรับการรักษาโรคมะเร็ง โดยเป็นเทคนิคที่ไม่รุกรานเซลล์ปกติ โดยการศึกษาใช้ข้อดีของผลกระทบของอะตอมหนักในการปรับเปลี่ยนโครงสร้างของสารเรืองแสงกลุ่มฟอร์มามาซาน เพื่อเพิ่มความสามารถในการข้ามระดับพลังงานระหว่างระดับชั้นพลังงานสถานะกระตุ้น เพื่อบรรลุเป้าหมายในการเพิ่มความสามารถในการสร้างออกซิเจนเชิงเดี่ยวที่สถานะกระตุ้นเพื่อประโยชน์ในการรักษาแบบใหม่ ในวิทยานิพนธ์นี้เสนอสองวิธีสำหรับการสังเกตการณ์การสร้างออกซิเจนเชิงเดี่ยวที่สถานะกระตุ้นที่ถูกส่งเสริมมาจากการข้ามระดับชั้นพลังงานที่ระดับชั้นพลังงานสถานะกระตุ้นของสารประกอบเชิงซ้อนที่ถูกสังเคราะห์ขึ้นมา โดยวิธีที่หนึ่งคือการติดตามการสลายตัวของ DPBF จากการสร้างออกซิเจนเชิงเดี่ยวที่สถานะกระตุ้น และวิธีที่สองเป็นการคำนวณเส้นโค้งพลังงานศักย์สำหรับกลไกปฏิกิริยาทางแสงของสารเรืองแสงโบรอนไดฟลูออไรด์ฟอร์มามาซาเนต โดยใช้วิธี DFT และ nudged elastic band (NEB) โดยในการทดลองนั้นพบว่าคุณสมบัติทางแสงที่ถูกศึกษาด้วยเทคนิคทางสเปกโทรสโกปี และการ X-ray ผลีกรวมไปถึงการคำนวณ DFT ซึ่งผลทางการทดลองทั้งในเชิงทฤษฎี และการทดสอบเซลล์ในหลอดทดลองได้ยืนยันความสามารถของสารไวแสงที่มีไอโอดีนติดอยู่ในการรักษาแมะเร็งผ่านการกระตุ้นด้วยแสงหรือที่เรียกว่าการรักษาแบบโฟโตไดนามิก

สาขาวิชาเคมี  
ปีการศึกษา 2567

ลายมือชื่อนักศึกษา

Tunyawat Khrootkaew

ลายมือชื่ออาจารย์ที่ปรึกษา

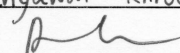


TUNYAWAT KHROOTKAEW : HEAVY ATOM EFFECT ON INTERSYSTEM CROSSING  
OF A BORON DIFLUORIDE FORMAZANATE COMPLEX-BASED PHOTSENSITIZER.  
THESIS ADVISER : ASSOC. PROF. ANYANEE KAMKAEW, Ph.D. 70 PP.

Keywords: Photodynamic therapy • Boron difluoride formazanate complex • Heavy atom effect • Singlet oxygen generation • TD-DFT

Photodynamic therapy (PDT) is a photochemical-based treatment approach that involves using light to activate photosensitizers (PSs). Attractively, PDT is one of the alternative cancer treatments due to its noninvasive technique. By utilizing the heavy atom effect, this work modified a class of formazan dyes to improve intersystem crossing (ISC) with the goal of enhancing reactive oxygen species (ROS) generation for PDT treatment. Two methods were used to observe the ROS generation enhanced by ISC of the synthesized complexes including, (i) recording DPBF decomposition caused by the ROS, and (ii) calculating the potential energy curves for photophysical mechanisms of  $\text{BF}_2$ -formazanate dyes using the DFT and nudged elastic band (NEB) methods. The photophysical properties of the dyes were studied using spectroscopic techniques and X-ray crystallography, as well as DFT calculations. The experimental and theoretical results and in vitro cellular assays confirmed the potential use of the newly synthesized iodinated  $\text{BF}_2$ -formazanate dyes in PDT.

School of Chemistry  
Academic Year 2024

Student's Signature Tunyawat Khrootkaew  
Advisor's Signature 

## ACKNOWLEDGEMENTS

This project was able to commence and succeed due to the invaluable assistance and excellent suggestions I received from professional researchers and highly skilled individuals with extensive experience. First, I would like to thank Assoc. Prof. Dr. Anyanee Kamkaew, my advisor, for drawing my attention to organic synthesis and providing insightful ideas and suggestions throughout this project. Second, I am grateful to Dr. Kantapat Chansaenpak, from the National Nanotechnology Center, for advising on photophysical properties. Third, I express my deepest gratitude to Prof. Dr. Kritsana Sagarik for guiding me with computational calculations and offering valuable recommendations. Additionally, I wish to thank my collaborators: Prof. Dr. Vinich Promarak, for optical and photoluminescence lifetime measurements; Asst. Prof. Dr. Worawat Wattanathana, for providing single-crystal X-ray data for characterization; and Asst. Dr. Piyanut Pinyou, for offering opportunities for electrochemical measurement. Furthermore, I extend my thanks to the Anyanee research group and the Computational Chemistry Research Laboratory (CCRL) for their unwavering assistance and support. Lastly, I am sincerely thankful to Suranaree University of Technology for providing laboratory space, chemicals, and tools for my research. The theoretical calculations were performed using the resources at [krypton.e-science.in.th](http://krypton.e-science.in.th) at the National Electronics and Computer Technology Center (NECTEC) and the Linux cluster at the Institute of Science, Suranaree University of Technology. This research was financially supported by Thailand Science Research and Innovation (TSRI) and the National Science, Research and Innovation Fund (NSRF) (NRIIS number 179313). Additionally, the Mid-Career Research Grant (N42A650389) from the National Research Council of Thailand (NRCT) was co-funded with the National Nanotechnology Center (P2250217).

Tunyawat Khrootkaew

# CONTENTS

	Page
ABSTRACT IN THAI.....	I
ABSTRACT IN ENGLISH.....	II
ACKNOWLEDGEMENTS .....	III
CONTENTS .....	IV
LIST OF TABLES .....	VI
LIST OF FIGURES .....	VII
LIST OF SCHEMES .....	XI
LIST OF ABBREVIATIONS.....	XII
<b>CHAPTER</b>	
<b>I INTRODUCTION.....</b>	<b>1</b>
1.1 Research objectives .....	2
1.2 Research hypothesis.....	2
1.3 Scopes .....	3
<b>II LITERATURE REVIEW.....</b>	<b>4</b>
2.1 Cancer disease .....	4
2.2 Photodynamic therapy in cancer treatment.....	5
2.3 Boron difluoride formazanate complex (BF <sub>2</sub> -Formazanate complex)....	6
2.4 Heavy atom effect in photodynamic therapy.....	7
<b>III RESEARCH METHODOLOGY .....</b>	<b>11</b>
3.1 Materials and instruments .....	11
3.2 Experiment protocol.....	11
3.3 Photophysical properties.....	15
3.4 Electrochemical measurement .....	16
3.5 Crystallographic measurement.....	16

## CONTENTS (Continued)

		Page
3.6	Computational method .....	17
3.6.1	DFT and TD-DFT calculations .....	17
3.6.2	Equilibrium geometries .....	17
3.6.3	Potential energy curves for rotational motions.....	18
3.7	<i>In Vitro</i> Cellular assays .....	18
3.7.1	Cell culture .....	18
3.7.2	Photodynamic therapy .....	19
3.7.3	LIVE/DEAD staining .....	19
3.7.4	Intracellular singlet oxygen generation .....	19
3.7.5	Apoptosis detection .....	20
<b>IV</b>	<b>RESULTS AND DISCUSSION .....</b>	<b>21</b>
4.1	Synthesis and Characterization of BF <sub>2</sub> -Formazanate complex .....	21
4.2	Photophysical properties of BF <sub>2</sub> -Formazanate complex .....	27
4.3	Single crystal X-ray diffraction .....	33
4.4	Electrochemical characterizations .....	38
4.5	Computational studies .....	39
4.6	Biological applications .....	53
<b>V</b>	<b>CONCLUSIONS.....</b>	<b>59</b>
	REFERENCE .....	60
	APPENDIX .....	68
	CURRICULUM VITAE .....	70

## LIST OF TABLES

Table	Page
4.1	Photophysical properties of BF <sub>2</sub> -Formazanate complexes..... 32
4.2	Crystal data and structure refinement details for two BF <sub>2</sub> -Formazanate complexes ( <b>BCI</b> and <b>BNI</b> )..... 35
4.3	The results of the Single-Crystal X-ray Diffraction Analysis for BF <sub>2</sub> -Formazanate Complexes <b>BCH</b> , <b>BNH</b> , <b>BCI</b> and <b>BNI</b> ..... 37
4.4	The calculated photophysical properties of BF <sub>2</sub> -Formazanate dyes in various solvents, using the equilibrium structures obtained from DFT/B3LYP/6-311G optimizations..... 43
4.5	The half maximal inhibitory concentration (IC <sub>50</sub> ) of <b>BCI</b> and <b>BNI</b> under various conditions..... 54

## LIST OF FIGURES

Figure	Page
2.1 The Jablonski diagram and pathway of PDT and ROS generation.....	5
2.2 The structure of the BODIPY(A) and BF <sub>2</sub> -Formazanate dye(B). ....	6
2.3 The arrangement of electron spins in the ground state, singlet excited state, and triplet excited state.....	7
2.4 The interconnection between singlet and triplet states, including their spin transitions.....	8
2.5 Controlling the intersystem crossing (ISC) rate by adjusting the energy gap between S <sub>1</sub> and T <sub>1</sub> states. According to Fermi's golden rule, reducing the singlet-triplet splitting energy ( $\Delta E_{ST}$ ) enhances ISC efficiency. ....	9
2.6 Enhancing the intersystem crossing rate by incorporating heavy atoms, which strengthen spin-orbit coupling (SOC) between singlet and triplet states, thereby promoting ISC. ....	10
4.1 <sup>1</sup> H-NMR of FCI.....	21
4.2 <sup>13</sup> C-NMR of FCI.....	22
4.3 HRMS of FCI.....	22
4.4 <sup>1</sup> H-NMR of FNI.....	22
4.5 <sup>13</sup> C-NMR of FNI.....	23
4.6 HRMS of FNI.....	23
4.7 <sup>1</sup> H-NMR of BCI.....	23
4.8 <sup>13</sup> C-NMR of BCI.....	24
4.9 <sup>19</sup> F-NMR of BCI.....	24
4.10 <sup>11</sup> B-NMR of BCI.....	24
4.11 HRMS of BCI.....	25
4.12 <sup>1</sup> H-NMR of BNI.....	25
4.13 <sup>13</sup> C-NMR of BNI.....	25

## LIST OF FIGURES (Continued)

Figure	Page
4.14 $^{19}\text{F}$ -NMR of <b>BNI</b> .....	26
4.15 $^{11}\text{B}$ -NMR of <b>BNI</b> .....	26
4.16 HRMS of <b>BNI</b> .....	26
4.17 The absorption (Solid line) and photoluminescence (dashed line) spectra of (A) <b>BCI</b> , (B) <b>BNI</b> , (C) <b>BCH</b> and (D) <b>BNH</b> in various solvents .....	29
4.18 The transient PL decay spectra of (A) <b>BCI</b> , (B) <b>BNI</b> , (C) <b>BCH</b> , and (D) <b>BNH</b> in various solvents. (The transient PL decay spectra of (E) <b>BCI</b> and <b>BNI</b> in solid state.).....	30
4.19 (A) Time-dependent UV-Vis absorbance change of DPBF with <b>BCI</b> , <b>BNI</b> , <b>BCH</b> , <b>BNH</b> , and Rose Bengal in DMSO under 532 nm light irradiation, and (B) UV-Vis absorbance changes of DPBF in degassed $\text{O}_2$ of $\text{H}_2\text{O}$ (3%Tween 80) solutions of <b>BCI</b> , <b>BNI</b> , <b>BCH</b> , <b>BNH</b> , and Rose Bengal irradiated with 532 nm light for 15 seconds. ....	31
4.20 Molecular structure of (A) <b>BCI</b> and (B) <b>BNI</b> , together with the atom-labeling scheme.....	34
4.21 Cyclic voltammograms of (A) non-iodinated complexes ( <b>BNH</b> and <b>BCH</b> ) and (B) iodinated complexes ( <b>BNI</b> and <b>BCI</b> ).....	39
4.22 The equilibrium structures of (A) <b>BCI</b> and (B) <b>BNI</b> in the $S_0$ , $S_1$ , and $T_1$ states in the gas phase ( $\epsilon = 1$ ). the torsional angle in degree represents $\omega_1$ and $\omega_2$ .....	40
4.23 HOMO and LUMO of the equilibrium structure of (A) <b>BCI</b> and (B) <b>BNI</b> in the $S_0$ state ( $\epsilon = 1$ ). (isosurface: 0.025).....	41
4.24 UV-vis absorption spectra of $\text{BF}_2$ -Formazanate complexes in various solvents obtained from theoretical and experimental methods .....	41
4.25 HOMO-LUMO of the equilibrium structures at ground state in COSMO of (A) <b>BCI</b> and (B) <b>BNI</b> . ( $\epsilon = 78$ , Isosurface: 0.025).....	42

## LIST OF FIGURES (Continued)

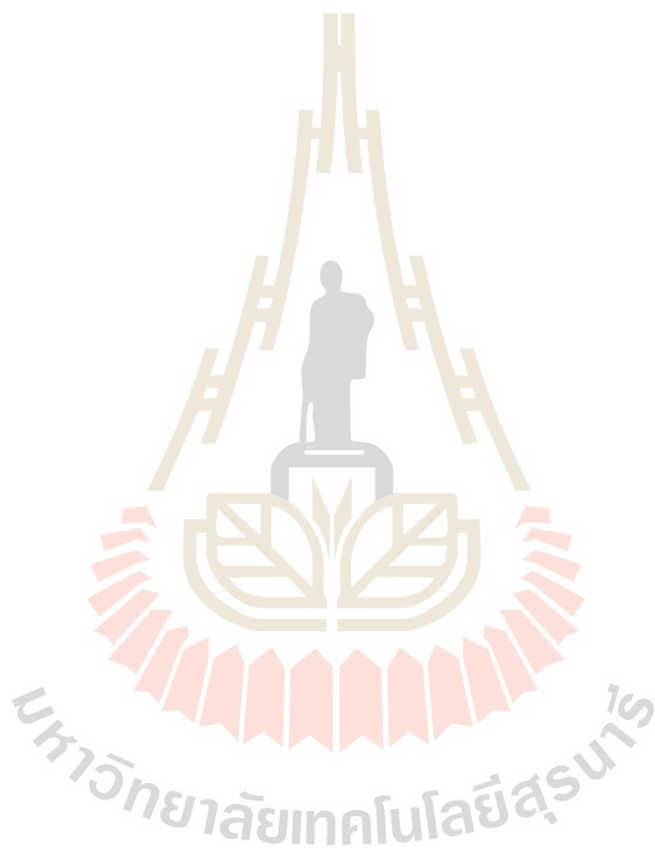
Figure	Page
4.26 The $S_0$ and $S_1$ potential energy curves for librational motions of both phenyl residues in <b>BCI</b> of <b>E-[1]<sup>*S1</sup></b> to <b>E-[2]<sup>eq,S1</sup></b> .....	44
4.27 The $S_0$ and $S_1$ potential energy curves for librational motions of both phenyl residues in <b>BCI</b> of <b>E-[2]<sup>eq,S1</sup></b> to <b>E-[3]<sup>S,S1</sup></b> .....	45
4.28 The $S_0$ and $T_1$ potential energy curves for librational motions of both phenyl residues in <b>BCI</b> of <b>E-[3]<sup>S,T1</sup></b> to <b>E-[4]<sup>eq,T1</sup></b> .....	46
4.29 The $S_0$ and $S_1$ potential energy curves for librational motions of both phenyl residues in <b>BNI</b> of <b>E-[1]<sup>*S1</sup></b> to <b>E-[2]<sup>eq,S1</sup></b> .....	47
4.30 The $S_0$ and $S_1$ potential energy curves for librational motions of both phenyl residues in <b>BNI</b> of <b>E-[2]<sup>eq,S1</sup></b> to <b>E-[3]<sup>S,S1</sup></b> .....	48
4.31 The $S_0$ and $T_1$ potential energy curves for librational motions of both phenyl residues in <b>BNI</b> of <b>E-[3]<sup>S,T1</sup></b> to <b>E-[4]<sup>eq,T1</sup></b> .....	49
4.32 The proposed mechanisms for excitation and radiation of <b>BCI</b> .....	51
4.33 The proposed mechanisms for excitation and radiation of <b>BNI</b> . .....	51
4.34 The proposed mechanisms for excitation and radiation of <b>BCH</b> .....	52
4.35 The proposed mechanisms for excitation and radiation of <b>BNH</b> .....	52
4.36 The relative cell viability of HepG2 cells under irradiation (0, 5, or 15 min) after incubation with (A) <b>BCI</b> or (B) <b>BNI</b> (0-50 $\mu$ M) for 24 h. Data are presented as means $\pm$ SD (n=3), *P <0.05, **P <0.01, or ***P <0.001 are based on Student's T-test. The $IC_{50}$ curves of (C) <b>BCI</b> and (D) <b>BNI</b> (0-50 $\mu$ M) treated on HepG2 cells followed by light irradiation (0, 5, or 15 min). .....	53
4.37 The fluorescent images of LIVE/DEAD co-staining assay of HepG2 cells after treatment with (A) <b>BCI</b> and (B) <b>BNI</b> (5 or 30 $\mu$ M) for 24 h then irradiation with light (15 min).....	55
4.38 The flow cytometry analysis of cells treated with <b>BCH</b> or <b>BNH</b> for 24 h, then stained with Calcein AM and PI compared with controls (cells no <b>BCH</b> or <b>BNH</b> treatment). .....	55

## LIST OF FIGURES (Continued)

Figure	Page
4.39 The intracellular ROS and $^1\text{O}_2$ detection in HepG2 cells using DCFH-DA and SOSG, respectively, after incubating the cells with <b>BCI</b> or <b>BNI</b> (10 $\mu\text{M}$ ) for 24 h followed by light illumination in comparison with dark conditions. Scale bars = 20 $\mu\text{m}$ . .....	56
4.40 The flow cytometry Annexin V fluorescein isothiocyanate (FITC)/ propidium iodide (PI) apoptosis analysis of cells incubated with <b>BCI</b> and <b>BNI</b> (10 $\mu\text{M}$ ) for 24 h.....	58
4.41 The flow cytometry Annexin V fluorescein isothiocyanate (FITC)/ propidium iodide (PI) apoptosis analysis of cells incubated with <b>BCH</b> and <b>BNH</b> (10 $\mu\text{M}$ ) for 24 h.....	58

## LIST OF SCHEMES

Scheme	Page
3.1 Photophysical properties of $\text{BF}_2$ -Formazanate complexes.....	13
3.2 Synthesis of $\text{BF}_2$ -Formazanate complexes.....	14



## LIST OF ABBREVIATIONSs

PDT	photodynamic therapy
ROS	reactive oxygen species
SOQY	singlet oxygen quantum yield
SOC	spin-orbital coupling
ISC	intersystem crossing
DFT	density functional theory
TD-DFT	time-dependent density functional theory
COSMO	conductor-like screening model
NEB	nudged elastic band
BODIPY	boron-dipyrromethene
TLC	thin-layer chromatography
TCSPC	time-correlated single-photon counting
TBAPF <sub>6</sub>	tetrabutylammonium hexafluorophosphate
CHCl <sub>3</sub>	Chloroform
THF	tetrahydrofuran
MeOH	methanol
DMSO	dimethyl sulfoxide
HepG2	liver hepatocellular carcinoma cancer cells
MTT	3-[4,5-dimethylthiazol-2-yl]-2,5 diphenyl tetrazolium bromide
NMR	nuclear magnetic resonance
DCFH-DA	2,7-dichloro-dihydrofluorescein diacetate
nm	nanometer
μm	micrometer
PI	Propidium Iodide
SOSG	singlet oxygen sensor green

# CHAPTER I

## INTRODUCTION

Cancer is a leading global cause of death, with around 10 million fatalities annually. Traditional treatments like surgery, chemotherapy, and radiotherapy face limitations such as tumor recurrence, invasiveness, and side effects due to poor targeting. Photodynamic therapy (PDT) offers a promising alternative, with improved specificity and reduced side effects. PDT involves activating photosensitizers with light, which react with oxygen to produce reactive oxygen species (ROS), inducing localized cytotoxicity. Over 500 PDT studies are underway, with some approved for cancer treatment. Advances in chemistry and nanotechnology have enhanced photosensitizers, boosting ROS production and PDT efficacy (S. Wang et al., 2023; Zhao et al., 2024).

Photodynamic therapy (PDT) is a cancer treatment strategy with advantages such as minimal invasiveness, high precision (Zhang et al., 2020), and the possibility of repetitive treatment of the affected area (Piskorz et al., 2021). PDT uses a photosensitizer (PS) that absorbs light to produce reactive oxygen species (ROS) including singlet oxygen ( $^1\text{O}_2$ ). Cellular oxygen ( $^3\text{O}_2$ ) absorbs energy released from the relaxation between the triplet excited state ( $T_n$ ) and ground state ( $S_0$ ) to generate  $^1\text{O}_2$  which is toxic to the cells. Two types of photosensitized reactions are involved with oxygen: type I and type II. In type I reactions, radicals are intermediates, transferring electron energy from the PS to the oxygen derivatives. In contrast, the PS transfers light energy directly to the oxygen in a type II reaction (Hak, Ravasaheb Shinde, and Rengan, 2021).

The boron difluoride ( $\text{BF}_2$ ) formazanate complexes are the novel classes of fluorescent dyes with intriguing applications in microscopy. (Sharma et al., 2020)  $\text{BF}_2$ -Formazanate complexes, similarly to BODIPY dyes, are composed of a " $\text{BF}_2$ " fragment coupled to a chelating N-donor ligand forming a stable six-membered heterocyclic ring. Despite their structural similarities,  $\text{BF}_2$ -Formazanate complex could be manufactured in two steps with readily accessible components. It is advantageous for many imaging

applications that BF<sub>2</sub>-Formazanate complexes exhibit a variety of photophysical features, such as strong molar extinction coefficients, large Stokes shifts, and high fluorescence quantum yield (Maar et al., 2015; Sharma et al., 2020). As widely reported, heavy atoms can improve the photosensitizer's singlet oxygen quantum yield (SOQY,  $\phi_{\Delta}$ ) by increasing the spin-orbital coupling (SOC) and the effect promotes intersystem crossing (ISC) rates, which is recognized as the heavy atom effect and thus it enhances the photodynamic therapeutic effect (Kamkaew et al., 2013; Miao et al., 2019; C. Wang and Qian, 2019; Zou et al., 2019). Moreover, most cases show the SOQY of the iodine atom higher than the bromine atom (Zou et al., 2017). To the best of our knowledge, there is no systematic study on the heavy atom effect on the BF<sub>2</sub>-Formazanate complexes for PDT applications. Therefore, in this study, we investigated the effect of iodine-substituted BF<sub>2</sub>-Formazanate dyes on facilitating the ISC process to T<sub>n</sub>.

### 1.1 Research objectives

This research aimed to develop a new PDT probe that can generate ROS with the aid of the heavy atom effect enhancement with the following objectives:

- 1) To synthesize and characterize **BCI**, **BNI**, **BCH** and **BNH**.
- 2) To evaluate the influence of heavy atom effect on the photophysical properties of iodinated-compounds and noniodinated-compounds.
- 3) To investigate the radiation mechanisms of excited iodinated and non-iodinated model compounds through computational calculations.

### 1.2 Research hypothesis

The introduction of iodine atoms to BF<sub>2</sub>-Formazanate backbone could promote intersystem crossing (ISC) phenomena leading to improved singlet oxygen-generating properties of the compound.

### 1.3 Scopes

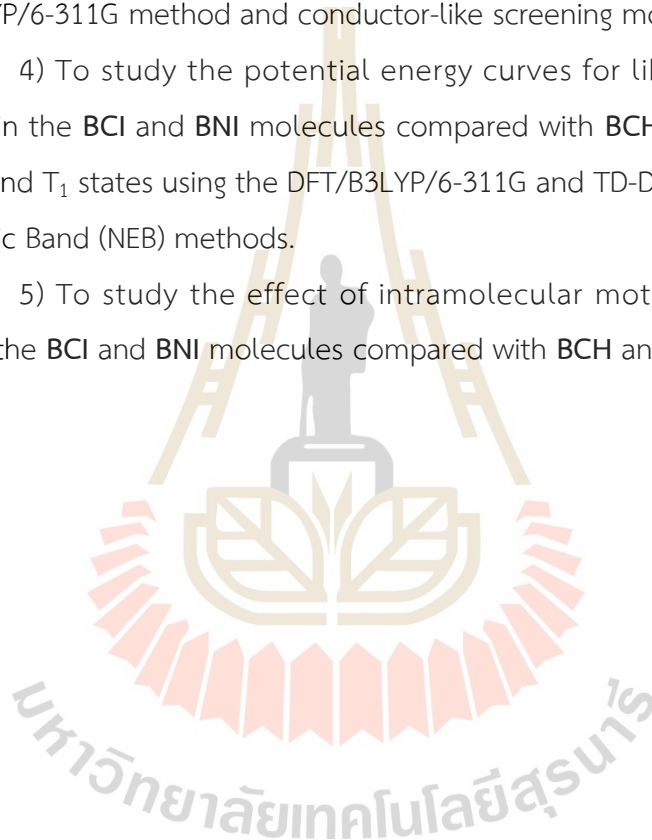
1) To synthesize and characterize **BCI**, **BNI**, **BCH** and **BNH** compounds shown in Schemes 3.1 and 3.2.

2) To study experimentally the photophysical properties of **BCI**, **BNI**, **BCH** and **BNH**.

3) To elucidate the equilibrium structures, energetics, and spectroscopic properties of **BCI** and **BNI** in several polar and nonpolar solvents using the DFT/B3LYP/6-311G method and conductor-like screening model (COSMO).

4) To study the potential energy curves for librational motions of phenyl rings in the **BCI** and **BNI** molecules compared with **BCH** and **BNH** molecules in the  $S_0$ ,  $S_1$  and  $T_1$  states using the DFT/B3LYP/6-311G and TD-DFT/B3LYP/6-311G and Nudged Elastic Band (NEB) methods.

5) To study the effect of intramolecular motion on the radiation processes in the **BCI** and **BNI** molecules compared with **BCH** and **BNH** molecules.



## CHAPTER II

### LITERATURE REVIEW

#### 2.1 Cancer disease

Cancer has become one of the leading causes of death globally, with the World Health Organization reporting approximately 10 million fatalities annually, making it the second most common cause of mortality. Traditional cancer treatments, such as surgery, chemotherapy, and radiotherapy, are widely used; however, their effectiveness is often hindered by challenges like tumor recurrence, invasiveness, and significant side effects due to poor tumor-specific targeting. These limitations have fueled the demand for alternative therapeutic approaches. Among these, photodynamic therapy (PDT) has emerged as a highly promising modality, offering improved target specificity and reduced side effects compared to conventional methods. PDT works by activating photosensitizers with light energy, which subsequently react with oxygen ( $O_2$ ) to produce reactive oxygen species (ROS) that induce localized cytotoxicity. This precision-driven therapy has garnered increasing interest in both fundamental research and clinical applications. According to data from ClinicalTrials.gov, over 500 PDT-related studies are either ongoing or completed, with some already approved for cancer treatment. Additionally, advancements in chemistry and nanotechnology have facilitated the development of enhanced photosensitizers, significantly improving ROS production and PDT efficacy. These innovations highlight PDT as a key player in the evolving landscape of precision cancer therapies, alongside other laser-based approaches like photothermal therapy (PTT), (S. Wang et al., 2023; Zhao et al., 2024).

## 2.2 Photodynamic therapy in cancer treatment

Photochemical reactions occur when light interacts with chemical molecules. In photochemical processes, photon energy is absorbed directly by the target molecule, which is called a photosensitizer, which could then transfer the energy onto the target molecule. Phototherapy is an alternative treatment for various human diseases, including cancer, rheumatoid arthritis, and psoriasis, using only light energy (photon). Photodynamic therapy (PDT) is a promising modality for noninvasive cancer treatment. Moreover, photodynamic therapy uses an external chemical (photosensitizer) that absorbs light energy and then produces singlet oxygen ( $^1\text{O}_2$ ) after exciting photosensitizers to a singlet excited state ( $S_n$ ). The cellular oxygen ( $^3\text{O}_2$ ) absorbs energy released from the relaxation between the triplet excited state ( $T_n$ ) and ground state ( $S_0$ ) to generate  $^1\text{O}_2$ . The photosensitizer (PS) turns on therapeutic effects in the presence of  $^1\text{O}_2$ , and its toxicity leads to cell death. Two types of photosensitized reactions are involved with oxygen: type I and type II. In type I reactions, radicals are intermediate, transferring electron energy from the photosensitizer to the oxygen derivatives. The photosensitizer passes light energy directly to the oxygen in a type II reaction (Hak et al., 2021). The pathway of PDT is shown in Figure 2.1, (Pham, Nguyen, Choi, Lee, and Yoon, 2021).

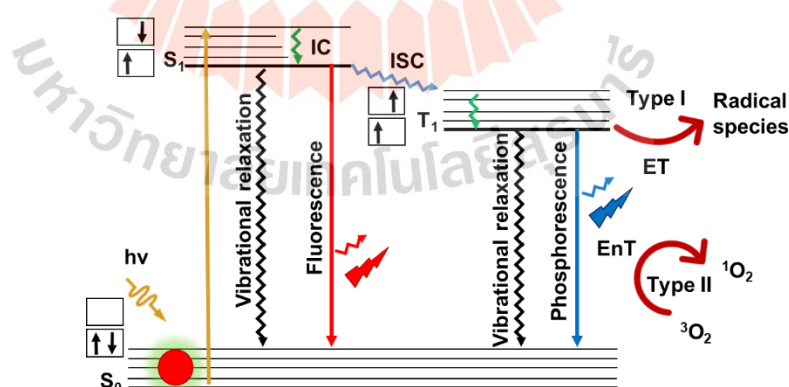


**Figure 2.1** The Jablonski diagram and pathway of PDT and ROS generation.

(IC: Internal conversion, ISC: Intersystem crossing)

### 2.3 Boron difluoride formazanate complex (BF<sub>2</sub>-Formazanate complex)

Boron difluoride (BF<sub>2</sub>) chelates of N-donor ligands are one of the most widely studied classes of molecular materials due to their unique, adjustable, and potentially beneficial absorption, emission, and electrochemical characteristics. These compounds, which include the ubiquitous boron dipyrromethenes (BODIPYs) shown in Figure 2.2A, have demonstrated utility as sensors, efficient electrochemiluminescence luminophores and functional components of organic electronics, in photodynamic therapy, and, perhaps most notably, as fluorescence cell imaging agents (Maar et al., 2015).

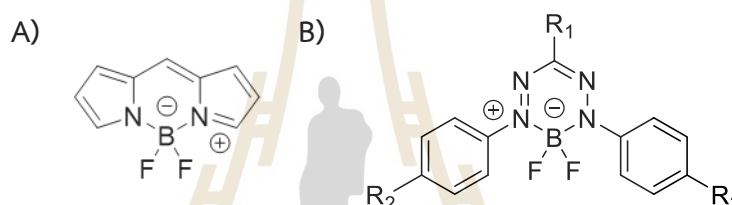


**Figure 2.2** The structure of the BODIPY(A) and BF<sub>2</sub>-Formazanate dye(B).

The boron difluoride (BF<sub>2</sub>) formazanate dyes (Figure 2.2B) are novel classes of fluorescent dyes with intriguing applications in microscopy (Sharma et al., 2020). BF<sub>2</sub>-Formazanate dyes, similarly to BODIPY dyes, are composed of a "BF<sub>2</sub>" fragment coupled to a chelating N-donor ligand forming a stable six-membered heterocyclic ring. Despite their structural similarities, BF<sub>2</sub>-Formazanate dye could be manufactured in two easy steps with readily accessible components. Due to BF<sub>2</sub>-Formazanate dyes exhibit varying photophysical properties, such as large molar extinction coefficients and high fluorescence quantum yield, generally in the far-red or near-infrared range, which is beneficial for many imaging applications (Sharma et al., 2020).

We have devised novel BF<sub>2</sub>-Formazanate dyes, which enabled us to perform insight into experimental and theoretical investigations of the optoelectronic properties of these compounds. Moreover, we described the synthesis of symmetric 1-cyano and 1-nitro- BF<sub>2</sub>-Formazanate dyes, which bear iodine to turn on photodynamic therapy. The nature of substituents (R<sub>2</sub>- and R<sub>3</sub>- substituents in Figure 2.2B) strongly affected the optical properties by introducing the electron-donating

substituent in this position, and it showed the largest quantum yield and long wavelength shift in the emission spectra. The differences in optical properties between Ph-, CN-, and NO<sub>2</sub>-substituted BF<sub>2</sub>-Formazanate were attributed primarily to the electron-withdrawing nature of the R<sub>1</sub> substituent shown in Figure 2.2B (NO<sub>2</sub> > CN >> Ph) (Lipunova, Fedorchenko, and Chupakhin, 2019).

## 2.4 Heavy atom effect in photodynamic therapy

Triplet excited states are challenging to generate through direct photoexcitation because intersystem crossing (ISC) from the first singlet excited state (S<sub>1</sub>) to the first triplet excited state (T<sub>1</sub>) is symmetry-forbidden, and large singlet–triplet energy splitting exists in their chromophores. The triplet state is characterized by two electrons in separate molecular orbitals with parallel spins, distinguishing it from the singlet state in terms of spin configuration and transition properties (Figure 2.3).

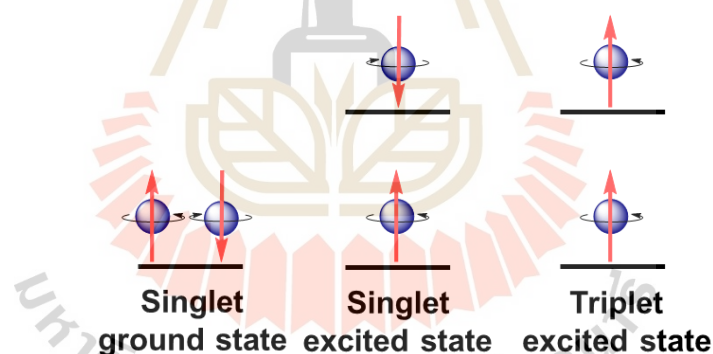


**Figure 2.3** The arrangement of electron spins in the ground state, singlet excited state, and triplet excited state.

Fluorescence occurs when a radiative transition takes place from the lowest singlet excited state to the singlet ground state, where both states share the same spin multiplicity. Conversely, phosphorescence is a radiative transition from the lowest triplet excited state to the singlet ground state. According to selection rules, transitions with identical multiplicity ( $\Delta S = 0$ ,  $2|S|+1$ ) are spin-allowed, whereas transitions with different multiplicity ( $\Delta S \neq 0$ ) are spin-forbidden (Figure 2.4).

However, a spin flip in a molecule's singlet excited state can activate the dark triplet state, making ISC possible (Figure 2.4) (Bao, Deng, Jin, and Liu, 2025). ISC, a nonradiative transition between electronic states with different spin multiplicities, is a key mechanism for converting singlet excited states into triplet excited states (Li, Kamasah, Matsika, and Suits, 2019) (Figure 2.4). The ISC rate can be significantly enhanced by heavy atoms (Galland et al., 2019; Yan, Lin, Sun, Ma, and Tian, 2021) as it is proportional to the eighth power of the atomic number (X. Wang et al., 2021).

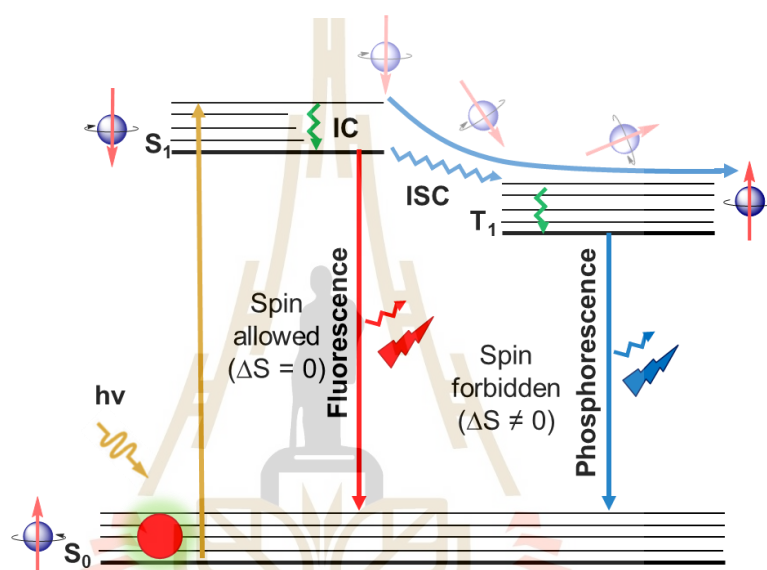
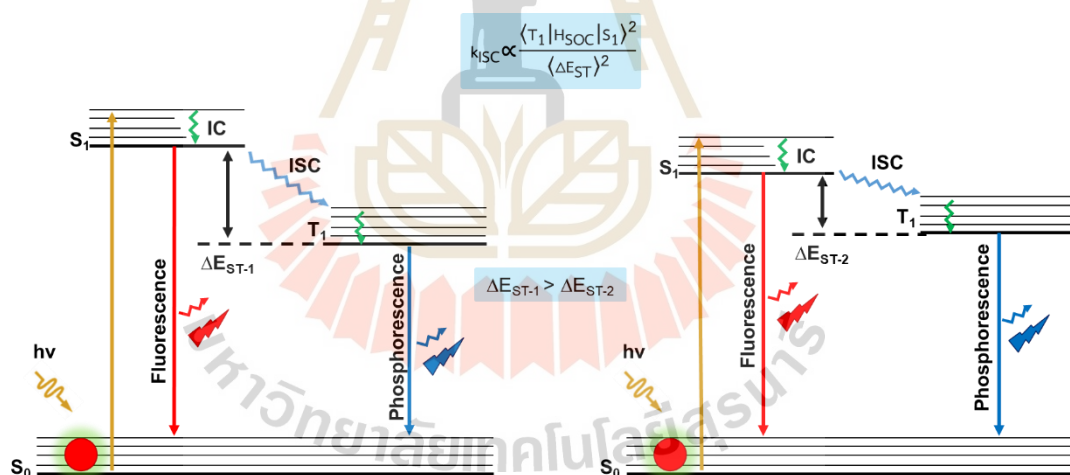


Figure 2.4 The interconnection between singlet and triplet states, including their spin transitions.

Chemical modifications of molecules can alter ISC efficiency by either reducing the singlet-triplet energy splitting  $\Delta E_{ST}$  or enhancing spin-orbit coupling (SOC). Triplet state regulation primarily depends on modulating the singlet–triplet splitting energy, which directly impacts ISC. The ISC rate ( $k_{ISC}$ ) follows Fermi’s golden rule (Xiao et al., 2021) as and is expressed in Equation (1):

$$k_{ISC} \propto \frac{\langle T_1 | H_{SOC} | S_1 \rangle^2}{\langle \Delta E_{ST} \rangle^2} \quad (1)$$

where  $\langle T_1 | H_{SOC} | S_1 \rangle$  represents the SOC constant, and  $\Delta E_{ST}$  is the singlet–triplet splitting energy. Reducing this energy gap enhances ISC rate (Figure 2.5). Additionally, increasing SOC achievable through heavy-atom incorporation further promotes ISC. The heavy-atom effect, which is proportional to the eighth power of atomic number (X. Wang et al., 2021), is one of the most effective methods for enhancing SOC (Hamzhepoor et al., 2023; Recio et al., 2022; Xiao et al., 2021).



**Figure 2.5** Controlling the intersystem crossing (ISC) rate by adjusting the energy gap between  $S_1$  and  $T_1$  states. According to Fermi’s golden rule, reducing the singlet–triplet splitting energy ( $\Delta E_{ST}$ ) enhances ISC efficiency. (Bao et al., 2025).

For example, substituting hydrogen atoms in the **AQCz** molecule with two heavier bromine atoms resulted in the derivative **AQCzBr<sub>2</sub>**, which exhibited a 2.8-fold increase in its SOC constant and an eightfold enhancement in  $k_{ISC}$  compared to the original **AQCz** molecule (Xiao et al., 2021) (Figure 2.6). A widely adopted strategy for developing efficient triplet-state photosensitizers is the incorporation of heavy atoms (e.g., iodine or bromine) into organic molecules (Hu, Zhang, and Liu, 2021). The heavy-atom effect improves SOC, thereby enhancing ISC and increasing the singlet oxygen quantum yield (SOQY). Notably, iodine-substituted compounds often exhibit higher SOQY than their bromine-substituted counterparts (Zou et al., 2017)

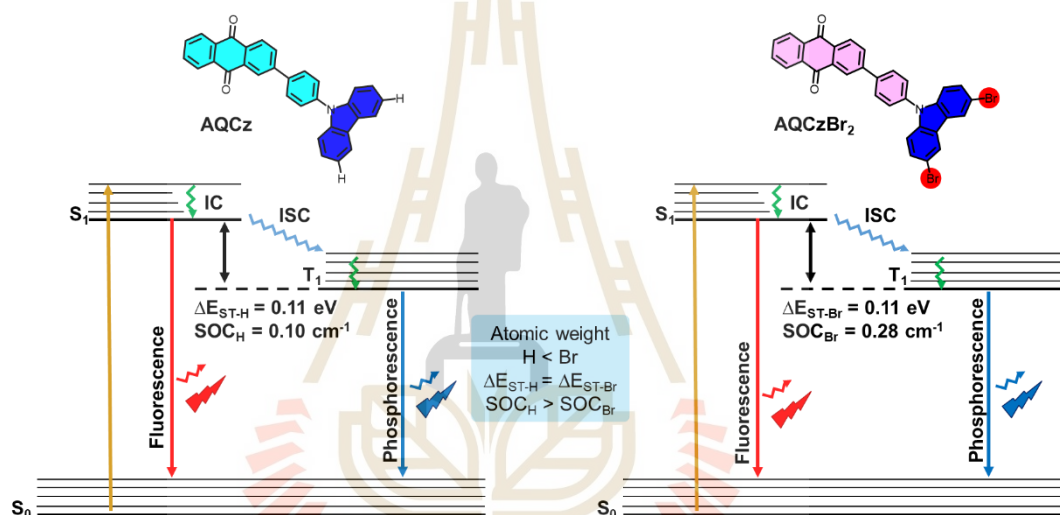


**Figure 2.6** Enhancing the intersystem crossing rate by incorporating heavy atoms, which strengthen spin-orbit coupling (SOC) between singlet and triplet states, thereby promoting ISC. (Modified diagram from this work (Xiao et al., 2021)).

Therefore, we proposed to synthesize and study the photophysical properties of **BCI** and **BNI** (structures shown in Figure 2.3A&B).

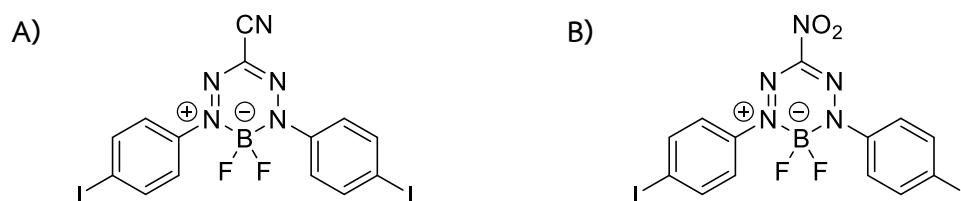


**Figure 2.7** The structures of the main target molecules in this work. **BCI** (A) and **BNI** (B).

## CHAPTER III

### RESEARCH METHODOLOGY

#### 3.1 Materials and instruments

All reagents and solvents were obtained from commercial sources (Sigma Aldrich, TCI, Carlo Erba, Acros, Merck) and used without further purification. The reaction was monitored by thin-layer chromatography (TLC) carried out on silica gel 60 F254 (Merck) and visualized under a UV cabinet. Column chromatography purifications were performed using silica gel and alumina gel for chromatography (Carlo Erba) as a stationary phase.  $^1\text{H-NMR}$ ,  $^{13}\text{C-NMR}$ ,  $^{11}\text{B-NMR}$ , and  $^{19}\text{F-NMR}$  spectra were recorded on Bruker-500 MHz spectrometer at room temperature. Chemical shifts of  $^1\text{H-NMR}$  and  $^{13}\text{C-NMR}$  spectra were reported in ppm from residue solvent peak as internal standard  $\text{CDCl}_3$  at  $\sim 7.26$  and  $\sim 77.16$  ppm, respectively. Splitting patterns are informed as singlet (s), doublet (d), triplet (t), multiplet (m), doublet of doublet (dd), and quartet (q). High-resolution mass spectrometry was measured by Electrospray Ionization (ESI) with negative mode in negative mode. The photophysical properties of  $\text{BF}_2$ -Formazanate complexes were investigated by Perkin Elmer Lambda 1050 UV/Vis/NIR spectrometer for Absorption spectra, and time-correlated single-photon counting (TCSPC) technique on Edinburgh Instruments FLS980 Spectrometer for emission spectra (PL) using excitation at 500 nm and fluorescence decay time, with a pulsed diode operating at  $\lambda_{\text{ex}} = 472.2$  nm. The instrument response function (IRF) was recorded.

#### 3.2 Experimental protocol

Preparation of formazans ( $\text{Ar}_1=\text{Ar}_5=\text{Ph}$ ,  $\text{R}_3=\text{CN}$  for **FCH**;  $\text{Ar}_1=\text{Ar}_5=\text{Ph}$ ,  $\text{R}_3=\text{NO}_2$  for **FNH**,  $\text{Ar}_1=\text{Ar}_5=p\text{-I-Ph}$ ,  $\text{R}_3=\text{CN}$  for **FCI**; and  $\text{Ar}_1=\text{Ar}_5=p\text{-I-Ph}$ ,  $\text{R}_3=\text{NO}_2$  for **FNI**) are shown in Scheme 3.1.

### Preparation of FCH and FCI

Cyanoacetic acid (1.7012 g, 20.0 mmol) and NaOH (1.76 g, 44.0 mmol) were dissolved in deionized water (100 mL), and the mixture was cooled down to 0 °C and stirred for 30 min. Afterward, concentrated HCl (12 M, 11.1 mL) was slowly added to a mixture of 4-iodoaniline for FCI (8.9798 g, 41.0 mmol) and deionized water (50 mL), then the solution was stirred at 0 °C for 15 min. Subsequently, NaNO<sub>2</sub> aqueous solution (2.4 M, 20 mL) cooled to 0 °C was added dropwise to the above 4-iodoaniline solution over 15 min. The obtained red/brown solution was stirred for 30 min, which was added dropwise to the prepared alkaline cyanoacetic acid solution for 15 min. The mixture was stirred for 3 h during which time and then neutralized with HCl (1 M). A dark red precipitate was formed and then filtered off to obtain the crude product. The resulting residue was purified by flash chromatography (CH<sub>2</sub>Cl<sub>2</sub>, neutral alumina) to yield FCI as a dark red solid. Yield=5.874 g, 57%.

FCH was synthesized as a dark orange solid (0.530 g, 10%) by following previously published protocols, and the NMR data were identical to those reported in the literature (Barbon, Reinkeluers, Price, Staroverov, and Gilroy, 2014).

FCI: <sup>1</sup>H NMR (500 MHz, CDCl<sub>3</sub>) δ 7.81 (d, J=8.1 Hz, 4H), 7.39 (d, J= 8.2 Hz, 4H), NH no detected. <sup>13</sup>C NMR (125 MHz, CDCl<sub>3</sub>) δ 139.1, 138.9, 124.5, 122.5, 99.1. HRMS (ESI -) m/z: the calculated value (calcd) for C<sub>14</sub>H<sub>8</sub>I<sub>2</sub>N<sub>5</sub> ([M-H]<sup>-</sup>): 499.8875, found: 499.8724.

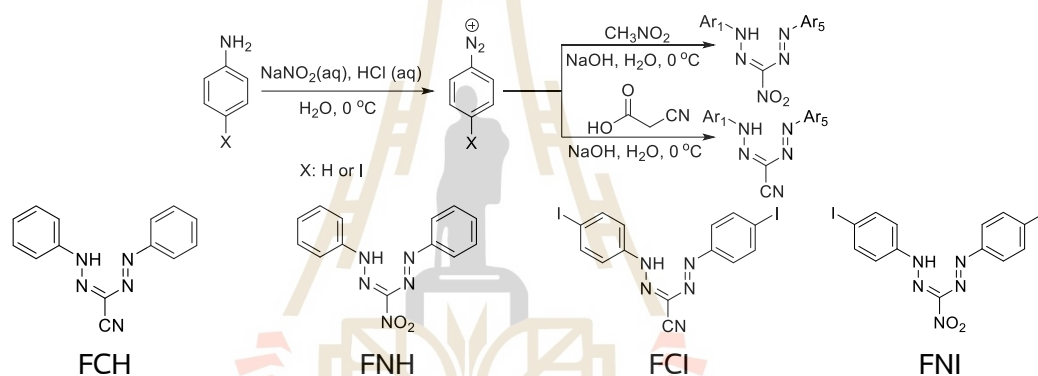
### Preparation of FNH and FNI

Nitromethane (1.23 mL, 20.0 mmol) and NaOH (1.76 g, 44.0 mmol) were dissolved in deionized water (100 mL), and the mixture was cooled down to 0 °C and stirred for 30 min. Afterward, concentrated HCl (12 M, 11.1 mL) was slowly added to a mixture of 4-iodoaniline for FNI (8.9798 g, 41.0 mmol) and deionized water (50 mL), then the solution was stirred at 0 °C for 15 min. Subsequently, NaNO<sub>2</sub> aqueous solution (2.4 M, 20 mL) cooled to 0 °C was added dropwise to the above 4-iodoaniline solution over 15 min. The obtained red/brown solution was stirred for 30 min, which was added dropwise to the prepared alkaline cyanoacetic acid solution for 15 min.

The mixture was stirred for 3 h during which time and then neutralized with HCl (1 M). A dark red precipitate was formed and then filtered off to obtain the crude product. The resulting residue was purified by flash chromatography ( $\text{CH}_2\text{Cl}_2$ , neutral alumina) to yield **FNI** as a dark red solid. Yield=1.700 g, 16%.

**FNH** was synthesized as a dark orange solid (0.241 g, 4%) by adapting previously published protocols and the NMR data were identical to those reported in the literature (Barbon, Staroverov, and Gilroy, 2015).

**FNI**:  $^1\text{H}$  NMR (500 MHz,  $\text{CDCl}_3$ )  $\delta$  7.84 (d,  $J=8.7$  Hz, 4H), 7.47 (d,  $J=8.3$  Hz, 4H), NH no detected.  $^{13}\text{C}$  NMR (125 MHz,  $\text{CDCl}_3$ )  $\delta$  145.9, 139.7, 139.2, 121.6, 96.3. HRMS (ESI  $-$ )  $m/z$ : the calculated value (calcd) for  $\text{C}_{13}\text{H}_{12}\text{N}_5\text{O}_2$ : 519.8873 ( $[\text{M}-\text{H}]^-$ ), found: 519.8731.



**Scheme 3.1** Synthesis of Formazans.

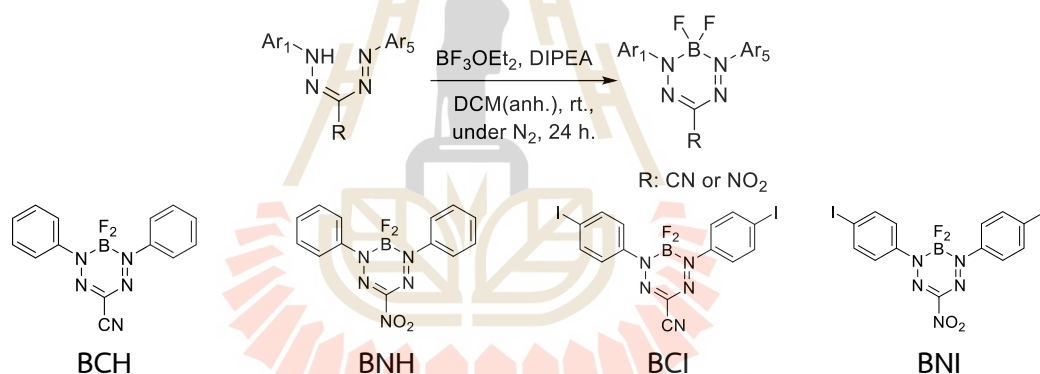
Preparation of  $\text{BF}_2$ -Formazanate complexes ( $\text{Ar}_1 = \text{Ar}_5 = p\text{-I-Ph}$ ,  $\text{R}_3 = \text{CN}$  for **BCI**;  $\text{Ar}_1 = \text{Ar}_5 = p\text{-I-Ph}$ ,  $\text{R}_3 = \text{NO}_2$  for **BNI** and  $\text{Ar}_1 = \text{Ar}_5 = \text{Ph}$ ,  $\text{R}_3 = \text{CN}$  for **BCH**;  $\text{Ar}_1 = \text{Ar}_5 = \text{Ph}$ ,  $\text{R}_3 = \text{NO}_2$  for **BNH**) are shown in Scheme 3.2

For all  $\text{BF}_2$ -Formazanate complexes use the same protocol. Formazans (0.5 g) were dissolved in dry dichloromethane (DCM) (50 mL). *N,N*-diisopropylethylamine, DIPEA (0.76 g, 0.78 mL, 5.88 mmol) was then added slowly, and the solution was stirred for 30 min. Boron trifluoride diethyl etherate (1.15 g, 1.15 mL, 8.10 mmol) was then stirred, for 24 h. The reaction mixture was then cooled to 20 °C and deionized water (10 mL) was added to quench any excess reactive boron-containing compounds. The solution was then extracted with deionized water (3 × 50 mL), dried over  $\text{MgSO}_4$ , gravity-filtered, and concentrated in vacuo.

The resulting residue was purified by flash chromatography (dichloromethane: hexane (2:8), silica gel) to afford BF<sub>2</sub>-Formazanate complexes (**BCI**, 0.374 g, yield = 68% and **BNI**, 0.348 g, yield = 64%) as dark purple microcrystalline solid). **BCH** and **BNH** were synthesized as dark red crystals (0.515 g, 87% and 0.173 g, 29%, respectively) by following previously published protocols and the NMR data were identical to those reported in the literature (Barbon et al., 2014; Barbon et al., 2015).

**BCI**: <sup>1</sup>H NMR (500 MHz, CDCl<sub>3</sub>) δ 7.86 (d, J = 9.0 Hz, 3H), 7.65 (d, J = 9.0 Hz, 4H). <sup>13</sup>C NMR (125 MHz, CDCl<sub>3</sub>) δ 142.7, 139.1, 124.5, 113.8, 99.1. <sup>11</sup>B NMR (161 MHz, CDCl<sub>3</sub>) δ -0.71 (t, J = 30.3 Hz). <sup>19</sup>F NMR (470 MHz, CDCl<sub>3</sub>) δ -132.11 (d, J = 30.3 Hz).

**BNI**: <sup>1</sup>H NMR (500 MHz, CDCl<sub>3</sub>) δ 7.89 (d, J = 8.9 Hz, 4H), 7.74 (d, J = 8.5 Hz, 4H). <sup>13</sup>C NMR (125 MHz, CDCl<sub>3</sub>) δ 142.9, 139.2, 124.7, 99.6. <sup>11</sup>B NMR (160 MHz, CDCl<sub>3</sub>) δ -0.59 (t, J = 30.1 Hz). <sup>19</sup>F NMR (470 MHz, CDCl<sub>3</sub>) δ -133.73 (dd, J = 59.7, 29.3 Hz).



Scheme 3.2 Synthesis of BF<sub>2</sub>-Formazanate complexes.

### 3.3 Photophysical properties

The UV-Vis absorption and emission spectra of compounds were measured in various solvents (Toluene, CHCl<sub>3</sub>, THF, and MeOH) with different polarities using a UV-vis spectrometer (Perkin-Elmer UV Lambda 1050 spectrometer).

Photoluminescence and lifetime were measured by steady state, fluorescence, and phosphorescence lifetime spectrometer FLS980 Edinburgh Instruments. Absolute quantum yield ( $\phi_{PL}$ ) was measured by integrating a sphere on an Edinburgh FLS980 spectrophotometer.

Singlet oxygen generation of BF<sub>2</sub>-Formazanate complexes was measured by adding 1,3-diphenylisobenzofuran (DPBF) 50  $\mu$ M into each solution of **BCI**, **BNI**, **BCH**, **BNH** and Rose Bengal (20  $\mu$ M) in DMSO. Then, the solution was irradiated with a UV-Vis lamp (532 nm) at a light intensity of 20 mW for 5 sec. Finally, absorbance intensities of the mixture solution were measured at an excitation of 532 nm using a UV-vis spectrometer (Shimadzu/UV-1900i, UV-vis spectrophotometer). Singlet oxygen quantum yield was calculated by this equation (2):

$$\phi_{\Delta} = \phi_{st} \left( \frac{\text{grad}_x}{\text{grad}_{st}} \right) \left( \frac{F_{st}}{F_x} \right) \quad (2)$$

$\phi_{st}$  =singlet oxygen quantum yield of the standard;  $\phi_{\Delta}$  =singlet oxygen quantum yield of unknown, and grad=slope of the best linear fit. F=absorption correction factor ( $F=1-10^{-\text{abs}}$ ; abs.= absorbance), and subscripts x and st=unknown and standard, respectively (Siriwibool et al., 2020).

### 3.4 Electrochemical measurement

Electrochemical properties of BF<sub>2</sub>-Formazanate complex analogues were studied by cyclic voltammetry in acetonitrile using a glassy carbon working electrode, and a platinum sheet counter electrode. Experiments were run at 100 mVs<sup>-1</sup> scan rate in degassed acetonitrile solutions of the analyte (~1 mM) and electrolyte (0.1 M tetrabutylammonium hexafluorophosphate (TBAPF<sub>6</sub>)). Cyclic voltammograms were referenced relative to the ferrocene/ferrocenium, (Fc/Fc<sup>+</sup>) redox couple (~1 mM internal standard), (Barbon et al., 2014).

### 3.5 Crystallographic measurement

Single crystals of BF<sub>2</sub>-Formazanate complexes (**BCI** and **BNI**) were obtained by slow evaporation of their solutions in the toluene solvent. The crystallographic measurements were taken by a Bruker D8 Venture diffractometer equipped with graphite-monochromated Cu-K $\alpha$  radiation. The absorption correction and data reduction were performed using SADABS (Sheldrick, 1996) and SAINT (SAINT Version 8.34A 2013; Bruker AXS: Madison, 2013), respectively. Employing Olex2 software (Dolomanov, Bourhis, Gildea, Howard, and Puschmann, 2009), the crystal structures were solved by SHELXT (Sheldrick, 2015b) and then refined by SHELXL (Sheldrick, 2015a). The non-hydrogen atoms were treated anisotropically, while the hydrogen atoms were refined using the riding model approximation. Mercury software (Macrae et al., 2006) was used to illustrate the molecular structures of the two BF<sub>2</sub>-Formazanate complexes. The crystal data of both compounds were deposited in the Cambridge Crystallographic Data Center with the deposition numbers (CCDC No.) of 2293556 for **BCI** and 2293557 for **BNI**.

## 3.6 Computational method

### 3.6.1 DFT and TD-DFT calculations

To study structural and spectroscopic properties of the  $\text{BF}_2$ -Formazanate complexes in the electronic ground ( $S_0$ ) and excited ( $S_1$  and  $T_1$ ) states, the density functional theory (DFT) and time-dependent density functional theory (TD-DFT) methods were applied with 6-311G basis set, abbreviated DFT/B3LYP/6-311G and TD-DFT/B3LYP/6-311G, (Kumar, Kołaski, Lee, and Kim, 2008; Siriwibool et al., 2020) respectively. Because photoexcitation processes generally break the symmetry of the excited molecules, DFT and TD-DFT calculations were performed only in C1 symmetry. The conductor-like screening model (COSMO) was used to account for the effects of solvent polarity, ranging from the gas phase to aqueous solutions ( $\epsilon = 1-78$ ). To study the internal conversion and intersystem crossing processes, the  $S_0$ ,  $S_1$ , and  $T_1$  states were considered in this work. All the DFT/B3LYP/6-311G and TD-DFT/B3LYP/6-311G calculations were performed using the TURBOMOLE 7.5 software package (Balasubramani et al., 2020; Kästner et al., 2009; Metz, Kästner, Sokol, Keal, and Sherwood, 2014).

### 3.6.2 Equilibrium geometries

The equilibrium geometries of **BCI** and **BNI** were optimized in the  $S_0$  state ( $\epsilon = 1-78$ ) using the DFT/B3LYP/6-311G method. Because preliminary DFT/B3LYP/6-311G calculations showed no strong solvent effect in the excited states, only  $\epsilon = 1$  was considered in the  $S_1$  and  $T_1$  state geometry optimizations. To assess the applied computational methods and to discuss the electron density distributions on the phenyl and heterocyclic rings, UV-vis spectra, and HOMO-LUMO of the equilibrium structures were computed and compared with available experimental data.

### 3.6.3 Potential energy curves for rotational motions

The potential energy curves for the intramolecular motions in the  $\text{BF}_2^-$  Formazanate complex were computed using the Nudged Elastic Band (NEB) method (Kästner et al., 2009; Sholl and Steckel, 2009). In this work, starting from the equilibrium structures of **BCI** and **BNI** in the  $S_0$  state, the potential energy curves for the two torsional motions were constructed in the  $S_1$  and  $T_1$  states. The potential energy curves concerning the dihedral angles ( $\omega_1$  and  $\omega_2$ ) were optimized in the range of -20– 180 degrees. The focus was on the probabilities for the internal conversion and intersystem crossing between  $S_1 \rightarrow S_0$  and  $S_1 \rightarrow T_1$ , as well as  $T_1 \rightarrow S_0$ . To study the probability of photoexcitation, the oscillator strengths (Osc.) were also computed along the potential energy curves. To study the effects of the torsional motions on the electron density distributions, the HOMO and LUMO of the characteristic structures were plotted along the  $S_0$ ,  $S_1$ , and  $T_1$  potential energy curves. All the NEB calculations were performed using the Limited-Memory Broyden-Fletcher-Goldfarb-Shanno (L-BFGS) optimizer included in the ChemShell software package (Kästner et al., 2009; Metz et al., 2014).

## 3.7 *In Vitro* Cellular assays

### 3.7.1 Cell culture

Liver hepatocellular carcinoma cancer cells (HepG2, ATCC) were cultured on a 75 cm<sup>2</sup> culture flask in Dulbecco's Modified Eagle Medium/ High glucose (DMEM/HIGH GLUCOSE, GE Healthcare Life Sciences HyClone Laboratories) supplemented with 10% fetal bovine serum (FBS, Gibco) and 1% Penicillin Streptomycin Solution 100X (CORNING) All the cells were cultured at 37°C in a humidified 95% air, 5% CO<sub>2</sub> atmosphere.

### 3.7.2 Photodynamic therapy

HepG2 cells were seeded into 96-well cell culture plates at  $1 \times 10^4$  cells per well and incubated in completed media for 24 h at 37°C under 5% CO<sub>2</sub>. After that, the cells were treated with 0, 2.5, 5, 10, 20, 30, and 50 μM of **BCI** and **BNI** in serum-free media, incubated for 24 h, and then the cells were washed with PBS 3 times. Thereafter, the cells were irradiated by a 532 nm lamp at 20 mW/cm<sup>2</sup> for 5 and 15 min and re-incubated for another 16 h. After incubation, the cells were washed with PBS (3 times) before being treated with methylthiazolyldiphenyl-tetrazolium bromide (MTT reagent 200 μL, 0.5 mg/mL, Sigma-Aldrich) for 2 h (Siriwibool et al., 2022). After reagent removal, DMSO was added to dissolve the formazan product, and the cell viabilities were determined through UV-vis absorption of the resulting formazan at wavelength 560 nm using a microplate reader (BMG Labtech/SPECTROstar Nano).

### 3.7.3 LIVE/DEAD staining

HepG2 cells were seeded into 96-well cell culture plates at  $3 \times 10^4$  cells/well and incubated for 24 h at 37°C under 5% CO<sub>2</sub>. Then, the media were replaced with **BCI** and **BNI** in DMEM with 5% FBS at concentrations of 0, 5, and 30 μM and the cells were incubated for 24 h. Thereafter, the cells were irradiated by a 532 nm lamp at 20 mW/cm<sup>2</sup> for 15 min and cells were re-incubated for another 16 h. After that, 4 μM calcein AM and propidium iodide (PI), (Thermo Fisher Scientific) were added to the tested cells for 5 min. (Siriwibool et al., 2020). Then all the cells were imaged using a fluorescence microscope (BioRad/Zoe); for calcein AM, 490 nm excitation and 515 nm emission filters were used; for PI, 535 nm excitation and 615 nm emission filters were used.

### 3.7.4 Intracellular singlet oxygen generation

HepG2 cells were seeded at a density of  $7 \times 10^3$  cells per well in 8-well Chambered Coverglass with non-removable wells and incubated for 24 h at 37°C under 5% CO<sub>2</sub>. After that, the cells were treated with 10 μM of **BCI** and **BNI** in DMEM

with 5% FBS before incubation for 24 h. Thereafter, the cells were washed with PBS (3 times) and re-incubated with 20  $\mu\text{M}$  of 2,7-dichloro-dihydrofluorescein diacetate (DCFH-DA, Sigma-Aldrich) and singlet oxygen sensor green (SOSG, Thermo Fisher Scientific) for 1 h (Siriwibool et al., 2022). Then the cells were washed with PBS (3 times) before being irradiated by a 532 nm lamp at 20  $\text{mW}/\text{cm}^2$  for 30 min and re-incubated for 10 min. After that, 1.0  $\mu\text{M}$  Hoechst 33342 (Thermo Fisher Scientific) was added to the cells before being imaged with LSCM. Fluorescence products of DCFH-DA, 2,7-dichloro-dihydro-fluorescein (DCF), and SOSG were detected by 488 nm excitation laser, and Hoechst 33342 was excited at 405 nm under Laser Scanning Confocal Microscope (Nikon A1Rsi). A 60 X oil immersion objective lens was used.

### 3.7.5 Apoptosis detection

HepG2 cells were seeded on a 6-well plate of approximately  $3 \times 10^5$  cells/well for 24 h. The cells were treated with **BCH**, **BNH**, **BCI**, or **BNI** (10  $\mu\text{M}$ ) in complete medium for 24 h. After incubation, the cells were then washed with 0.01 M PBS 3 times. After that, the cells were irradiated by a 532 nm lamp at 20  $\text{mW}/\text{cm}^2$  for 15 min and reintubated for another 24 h. To harvest the cells, the cells were trypsinized and washed three times with iced-cold 0.01 M PBS buffer (pH 7.4) by centrifugation at 4000 rpm at 4°C for 5 min. Thereafter, the cells were resuspended in 0.5 mL of 1X Annexin binding buffer, Thermo Fisher Scientific from Tali™ Apoptosis Kit). Then, 25  $\mu\text{L}$  of Annexin V fluorescein conjugate (Annexin V Alexa Flour™<sup>488</sup>, Thermo Fisher Scientific from Tali™ Apoptosis Kit) was added to resuspending cells and incubated at room temperature for 15 min before adding 2  $\mu\text{L}$  of 1 mg/mL Propidium iodide (PI, Sigma-Aldrich) on ice. The cells were kept on ice during the flow cytometry process. Then,  $1 \times 10^4$  events were analyzed by flow cytometry using an Attune NxT Flow Cytometer (Thermo Fisher Scientific).

## CHAPTER IV

### RESULTS AND DISCUSSION

#### 4.1 Synthesis and Characterization of BF<sub>2</sub>-Formazanate Complex

The synthesis part consists of **BCI** and **BNI** which were iodinated compounds and **BCH** and **BNH** which were non-iodinated compounds used as a control. All compound structures were characterized by <sup>1</sup>H, <sup>13</sup>C, <sup>11</sup>B and <sup>19</sup>F NMR via the chemical shift ( $\delta$ , ppm), resonance splitting, coupling constants (J), and number of protons. Moreover, the BF<sub>2</sub>-Formazanate complex series was confirmed by its mass-to-charge ratio (m/z) to present the exact molecular weight by high-resolution Electrospray Ionization Time of Flight mass spectroscopy (high-resolution ESI-TOF-MS). The results were elucidated to ensure the chemical structure of BF<sub>2</sub>-Formazanate complex series which is shown in Figure 4.1-4.16.

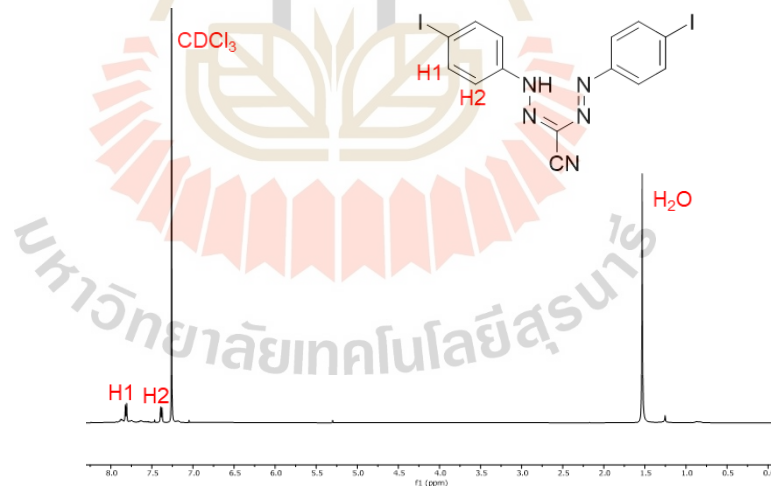


Figure 4.1 <sup>1</sup>H-NMR of FCI.

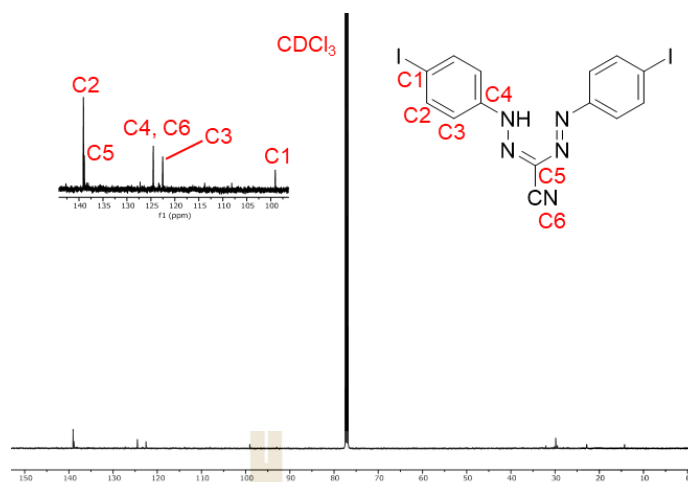
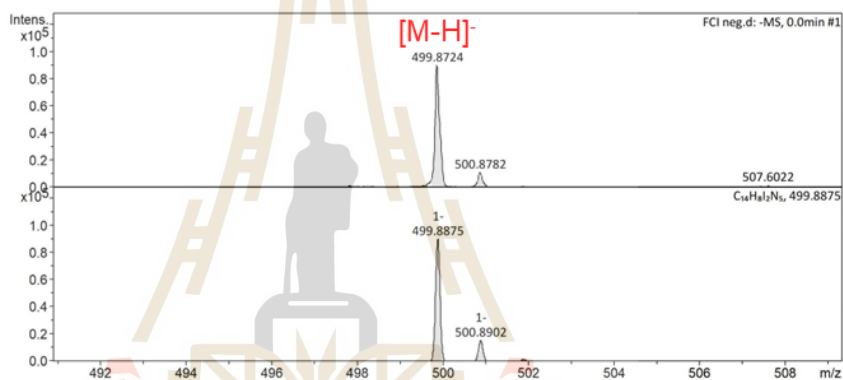
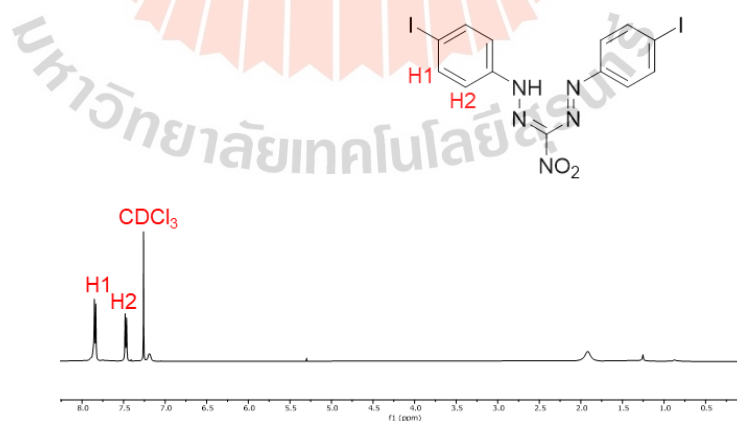
Figure 4.2  $^{13}\text{C}$ -NMR of FCI.

Figure 4.3 HRMS of FCI.

Figure 4.4  $^1\text{H}$ -NMR of FNI.

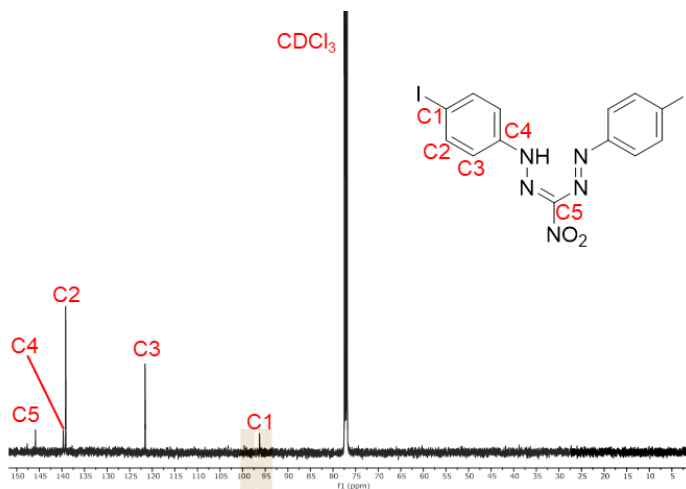
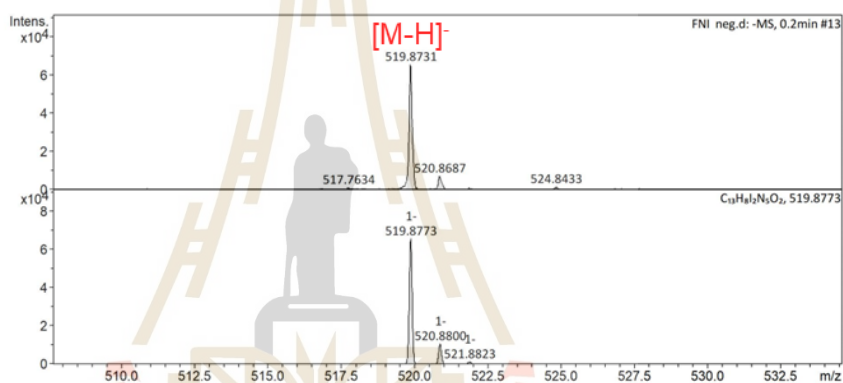
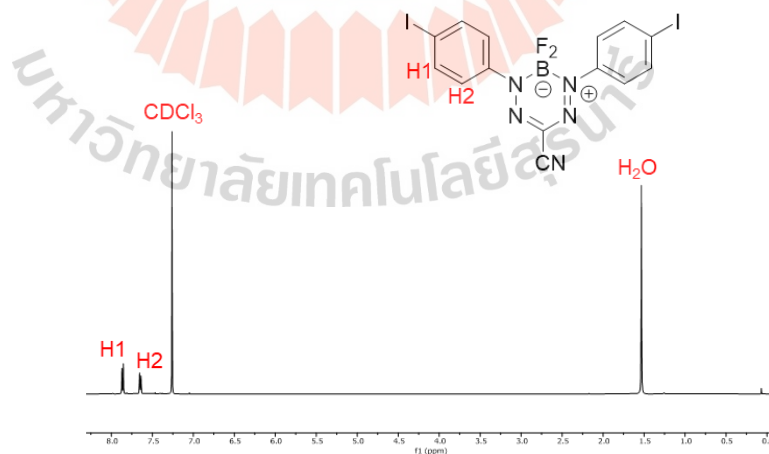
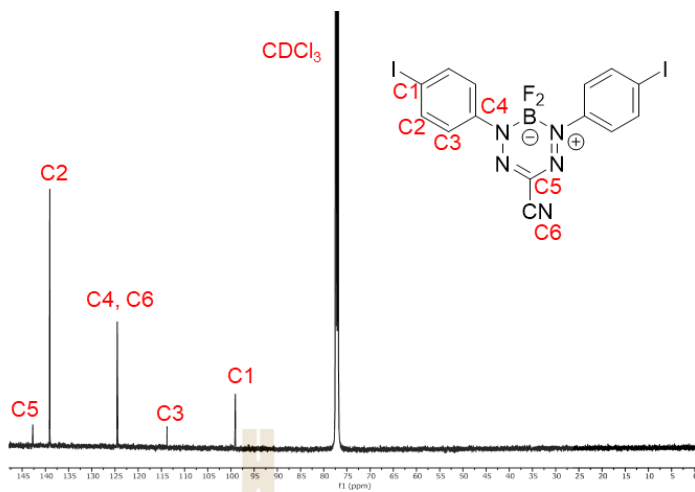
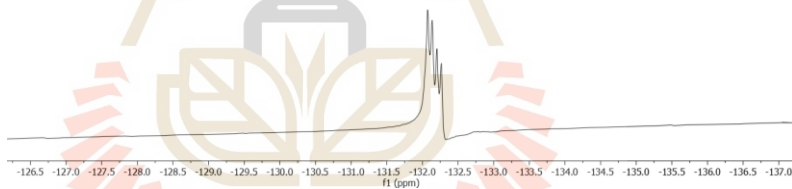
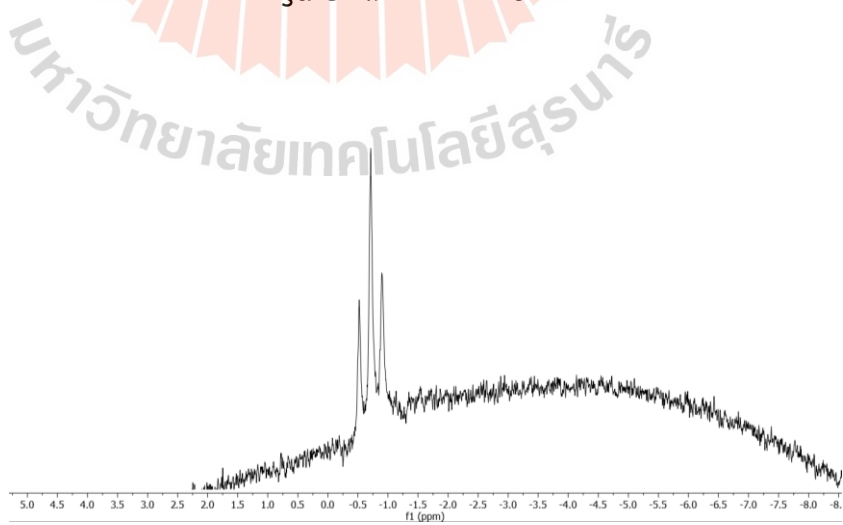
Figure 4.5  $^{13}\text{C}$ -NMR of FNI.

Figure 4.6 HRMS of FNI.

Figure 4.7  $^1\text{H}$ -NMR of BCI.

Figure 4.8  $^{13}\text{C}$ -NMR of BCI.Figure 4.9  $^{19}\text{F}$ -NMR of BCI.Figure 4.10  $^{11}\text{B}$ -NMR of BCI.

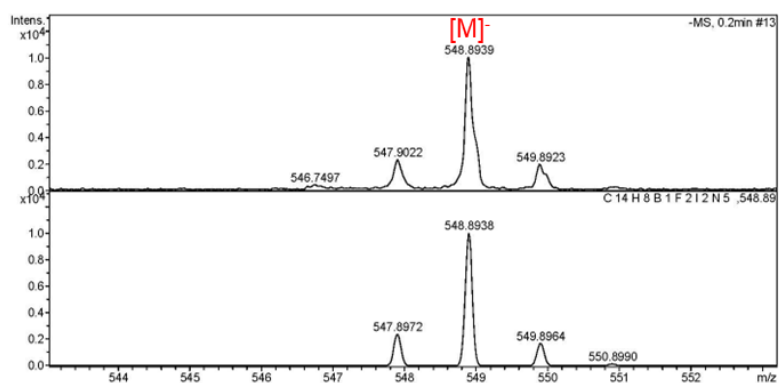
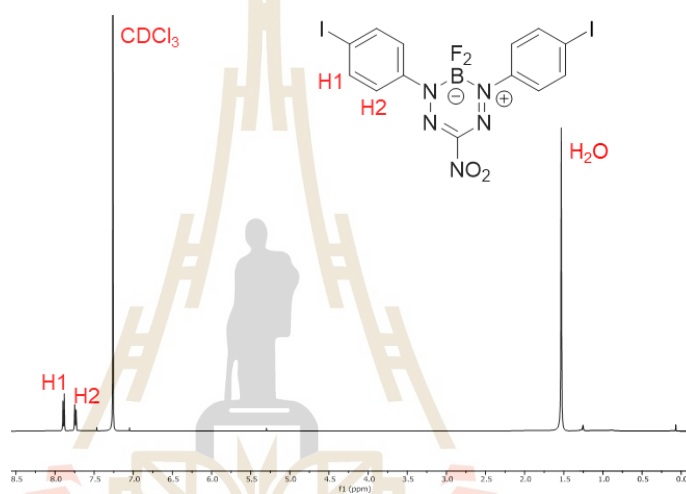
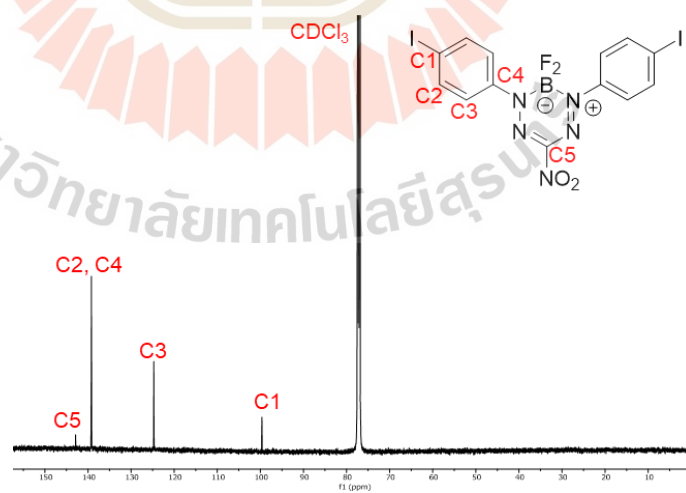


Figure 4.11 HRMS of BNI.

Figure 4.12  $^1\text{H-NMR}$  of BNI.Figure 4.13  $^{13}\text{C-NMR}$  of BNI.

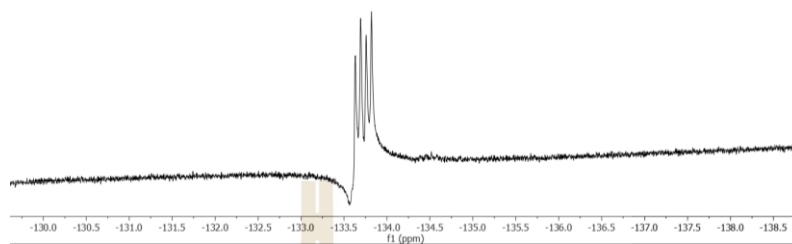
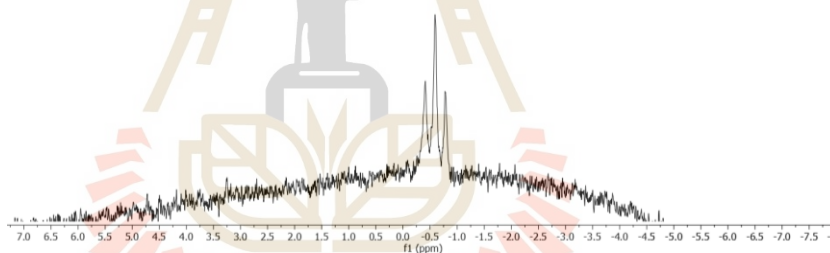
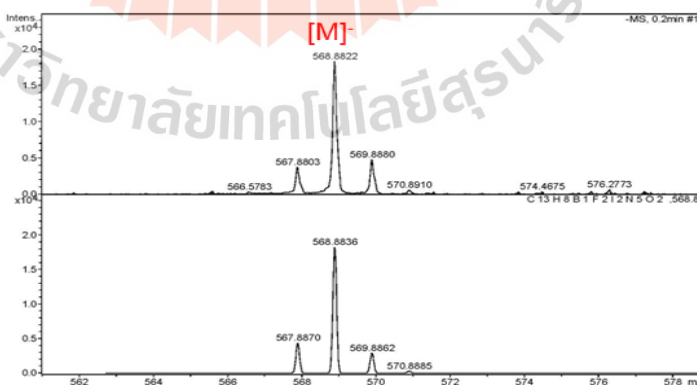
Figure 4.14  $^{19}\text{F}$ -NMR of BNI.Figure 4.15  $^{11}\text{B}$ -NMR of BNI.

Figure 4.16 HRMS of BNI.

## 4.2 Photophysical properties of BF<sub>2</sub>-Formazanate complex

The absorption and photoluminescence spectra of iodinated and noniodinated BF<sub>2</sub>-Formazanate complexes, **BCI**, **BNI**, **BCH**, and **BNH**, were measured in various solvents, as shown in Figure 4.17. **BCI** exhibited maximum absorption in the range of 495–537 nm, while **BNI** showed absorption maxima between 495–540 nm (Table 4.1). Notably, both compounds displayed bathochromic-shifted absorption in low-polar aprotic solvents, such as toluene. Furthermore, **BCI** and **BNI** exhibited large Stokes shifts, ranging from 98–184 nm for **BCI** and 100–190 nm for **BNI**, making them highly suitable for bioimaging applications (Table 4.1). Fluorophores with such large Stokes shifts (>80 nm) have minimal overlap between their absorption and emission spectra, reducing self-quenching via reabsorption and making them excellent light emitters for bioimaging applications (Chen et al., 2022; Sednev, Belov, and Hell, 2015). This property also minimizes interference between excitation and scattered light, enhancing signal-to-noise ratios, imaging specificity, and ROS generation. When compared to other BF<sub>2</sub>-complex families, such as BODIPY, BF<sub>2</sub>-Formazanate complexes, etc. show even larger Stokes shifts, adding to their bioimaging potential (Gilroy and Otten, 2020; Loudet and Burgess, 2007).

In addition, Both **BCI** and **BNI** exhibited high emission spectra in aprotic solvents such as toluene and chloroform while demonstrating moderate emissive signals in polar protic solvents such as tetrahydrofuran and methanol which are consistent with their absolute photoluminescence quantum yield values (Table 4.1). Distinctly, both complexes showed low fluorescent signal in the high polar aprotic solvent, DMSO (Table 4.1), which is the typical photophysical properties of fluorescent dyes containing electron donor and acceptor units (Aryamueang et al., 2022; Hiranmartsuwan et al., 2022; Nootem et al., 2020). Compared to their non-iodinated analogs (**BCH** and **BNH**), **BCI** and **BNI** display bathochromic-shifted absorption, emission maxima along with strong absolute photoluminescence quantum yield, and long PL lifetimes decay which could be the result of heavy atom effect of iodine atoms (Table 4.1). Additionally, both complexes exhibit transient PL lifetimes decay

(3.6 ns for **BCI** and 3.4 ns for **BNI** in solid state) indicating that the type of electron-withdrawing substituents (cyano and nitro groups) has negligible effect on the photoluminescent emissive properties of the compounds (Figure 4.18E).

The singlet oxygen quantum yields (SOQY;  $\phi_{\Delta}$ ) of the iodinated BF<sub>2</sub>-Formazanate complexes (**BCI** and **BNI**) were also evaluated and compared to their non-iodinated analogs (**BCH** and **BNH**) to assess the impact of iodine substitution on singlet oxygen generation. The singlet oxygen production was quantified using 1,3-diphenylisobenzofuran (DPBF), and the corresponding SOQYs were calculated using Rose Bengal as the standard ( $\phi_{\Delta} = 0.76$  in DMSO), (Gandra et al., 2006). DPBF played a role as a <sup>1</sup>O<sub>2</sub> scavenger and had zero absorption overlaps with **BCI**, **BNI**, **BCH**, **BNH**, and Rose Bengal, ensuring accurate analysis. Rose Bengal was selected due to its well-documented SOQY value and absorption profile, which is comparable to the BF<sub>2</sub>-Formazanate complexes (DeRosa and Crutchley, 2002; Redmond and Gamlin, 1999). As shown in Figure 4.19A, the absorbance of DPBF decreased significantly in the presence of **BCI** and **BNI** under 532 nm irradiation, confirming singlet oxygen generation. In contrast, the absorbance of DPBF in the presence of **BCH** and **BNH** remained unchanged. The SOQY values calculated using Equation 2 (Photophysical Properties section) showed a dramatic increase for **BCI** ( $\phi_{\Delta} = 7.4\%$ ) and **BNI** ( $\phi_{\Delta} = 5.6\%$ ) compared to **BCH** ( $\phi_{\Delta} = 0.2\%$ ) and **BNH** ( $\phi_{\Delta} = 0.6\%$ ), demonstrating that iodine substitution enhances singlet oxygen generation by 37-fold and 9.3-fold for **BCI** and **BNI**, respectively. Interestingly, the absorption spectra of **BCI**- and **BNI**-containing solutions remained unchanged after 30 seconds of irradiation at 532 nm, suggesting that the photosensitizers (PSs) are stable under these conditions. The observed reduction in DPBF absorbance upon irradiation confirmed the generation of singlet oxygen by **BCI** and **BNI**. In control experiments with degassed solutions, no changes in DPBF absorbance were detected, indicating that singlet oxygen production requires the presence of molecular oxygen (Figure 4.19B). These results demonstrated that incorporating iodine atoms into the formazanate backbone significantly promotes intersystem crossing (ISC) through the heavy atom effect, thereby improving

the singlet oxygen generation efficiency of these compounds and confirmed the iodinated BF<sub>2</sub>-Formazanate complex was a type-II PDT agent (Zou et al., 2017).

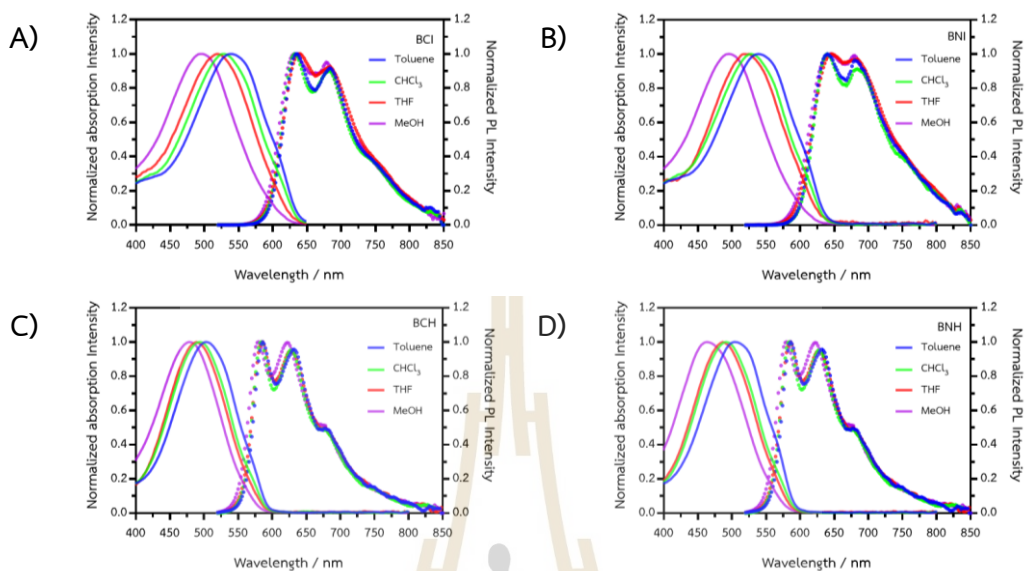


**Figure 4.17** The absorption (Solid line) and photoluminescence (dashed line) spectra of (A) BCI, (B) BNI, (C) BCH and (D) BNH in various solvents.

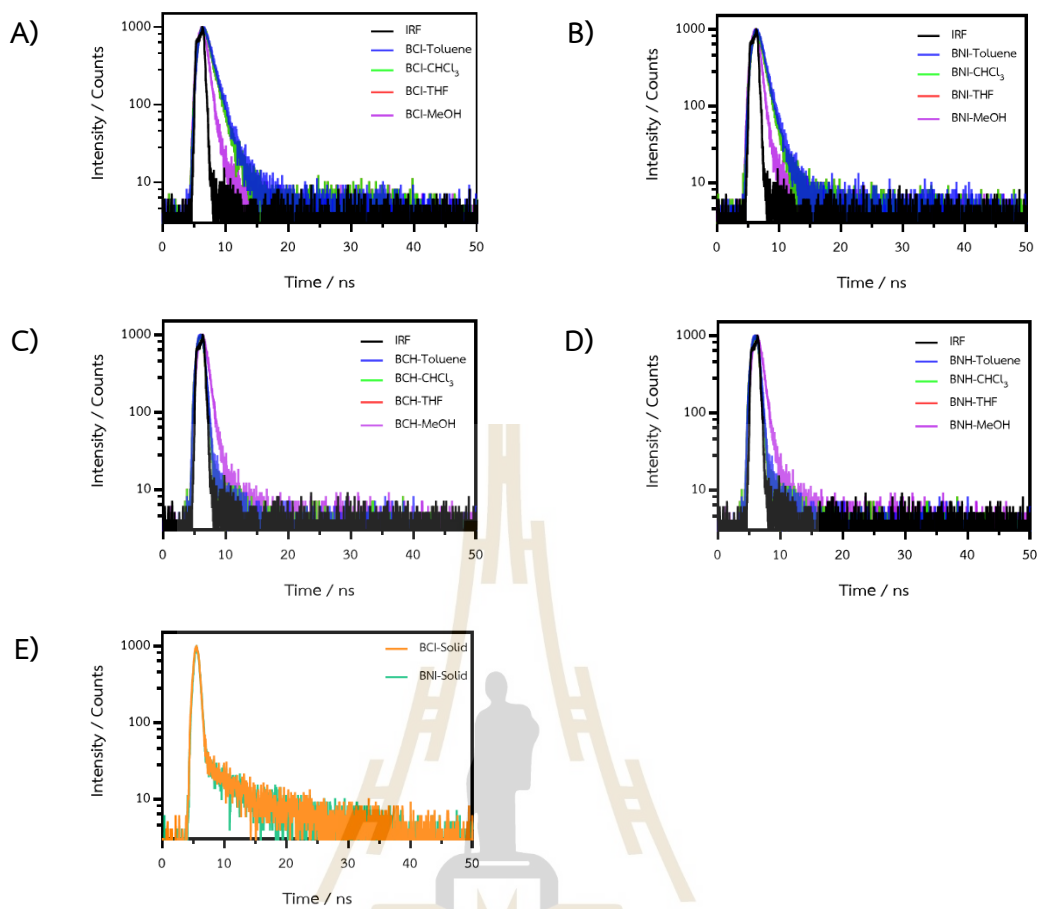


Figure 4.18 The transient PL decay spectra of (A) BCI, (B) BNI, (C) BCH, and (D) BNH in various solvents. (The transient PL decay spectra of (E) BCI and BNI in solid state.)

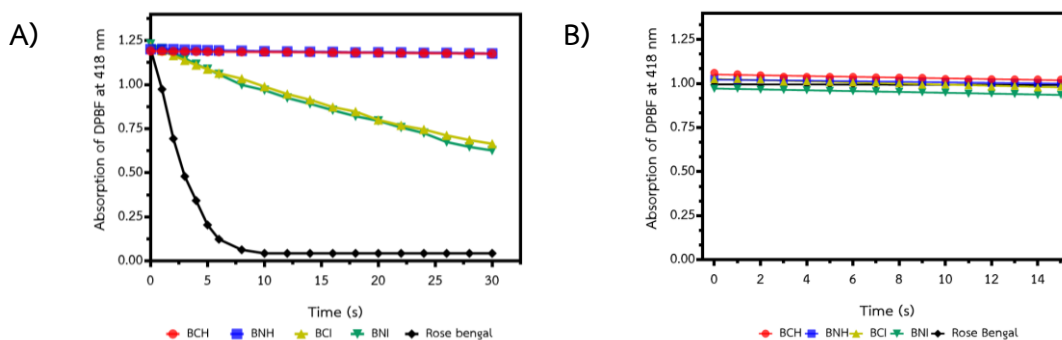


Figure 4.19 (A) Time-dependent UV-Vis absorbance change of DPBF with BCI, BNI, BCH, BNH, and Rose Bengal in DMSO under 532 nm light irradiation, and (B) UV-Vis absorbance changes of DPBF in degassed O<sub>2</sub> H<sub>2</sub>O (3% Tween 80) solutions of BCI, BNI, BCH, BNH, and Rose Bengal irradiated with 532 nm light for 15 seconds.

**Table 4.1** Photophysical properties of BF<sub>2</sub>-Formazanate complexes.

CPD	Solvent	$\lambda_{\text{Abs}}^{[a]}$	$\epsilon_{\text{A}}^{[b]}$	$\lambda_{\text{PL}}^{[c]}$	$\tau^{[d]}$	$\phi_{\text{PL}}^{[e]}$	$\phi_{\text{F}}^{[f]}$	$\phi_{\Delta}^{[g]}$
<b>BCI</b>	Toluene	537	1.31	635, 685	2.26	38	51	-
	CHCl <sub>3</sub>	527	0.84	631, 681	1.31	40	48	-
	THF	518	1.04	637, 684	1.20	14	-	-
	MeOH	495	0.82	631, 679	<1.00	11	22	-
	DMSO	-	-	-	-	-	1	7.4
<b>BNI</b>	Toluene	540	1.35	640, 680	1.21	55	42	-
	CHCl <sub>3</sub>	528	0.87	640, 685	1.11	40	38	-
	THF	521	0.63	645, 685	1.0	10	-	-
	MeOH	495	1.08	643, 685	<1.00	3	15	-
	DMSO	-	-	-	-	-	1	5.6
<b>BCH</b>	Toluene	501	1.46	585, 633	1.43	18	-	-
	CHCl <sub>3</sub>	493	1.83	583, 630	1.31	20	-	-
	THF	489	1.32	585, 627	1.10	3	-	-
	MeOH	478	1.53	586, 622	<1.00	3	-	-
	DMSO	-	-	-	-	-	-	0.2
<b>BNH</b>	Toluene	504	1.35	588, 631	<1.00	18	-	-
	CHCl <sub>3</sub>	490	1.70	586, 630	<1.00	19	-	-
	THF	485	1.21	587, 626	<1.00	1	-	-
	MeOH	464	1.25	582, 624	<1.00	1	-	-
	DMSO	-	-	-	-	-	-	0.6

<sup>[a]</sup> $\lambda^{\text{abs}}$  = absorption maximum wavelength; nm, <sup>[b]</sup> $\epsilon_{\text{A}}$  = molar absorptivity; \*10<sup>4</sup> M<sup>-1</sup>cm<sup>-1</sup>, <sup>[c]</sup> $\lambda_{\text{PL}}$  = photoluminescence maximum wavelength; nm (Excitation  $\lambda^{\text{abs}}$ ), <sup>[d]</sup> $\tau$  = transient photoluminescence decay lifetime; ns, <sup>[e]</sup> $\phi_{\text{PL}}$  = absolute photoluminescence quantum yield; %, <sup>[f]</sup> $\phi_{\text{f}}$  = Fluorescence quantum yields calculated in relative with fluorescein in 0.1 M NaOH ( $\phi_{\text{f}}$  = 95); %, <sup>[g]</sup> $\phi_{\Delta}$  = Singlet oxygen quantum yields

### 4.3 Single crystal X-ray diffraction

The structures of two  $\text{BF}_2$ -Formazanate complexes (**BCI** and **BNI**) were confirmed by single-crystal X-ray diffraction (Figure 4.20). Their crystal data and corresponding refinement details are tabulated in Table 4.2. The compound **BCI** crystallized into a monoclinic  $C2/c$  space group, while **BNI** formed a  $P-1$  triclinic crystal. The asymmetric unit of the compound **BCI** contained only half of its molecule due to the presence of 2-fold rotation symmetry. On the contrary, the asymmetric unit of the compound **BNI** was comprised of its whole molecule as a triclinic crystal system that did not possess rotational symmetry. For both compounds, the boron atom adopts a distorted tetrahedral geometry, where B-F bonds are shorter than B-N bonds (Nootem et al., 2021). The bonds regarding the  $\text{BF}_2$ -Formazanate complexes moiety of the two compounds, namely B-N, B-F, N-N, and N-C, were similar, indicating that the substituent groups on the *N*-aryl rings had a slight effect on the molecular structure of  $\text{BF}_2$ -Formazanate complexes. Compared to the bond lengths (Å) and angles (deg) in the complexes without iodine (**BCH** and **BNH**), (Barbon et al., 2015) the results indicate that iodine has little effect on the bond lengths of the *N*-aryl rings; most of the values are unaffected (Table 4.3). In the case of **BNH** and **BNI**, moderately different degrees of twisting (1–3 deg) were observed between *N*-aryl substituents and the backbone of the formazanate.

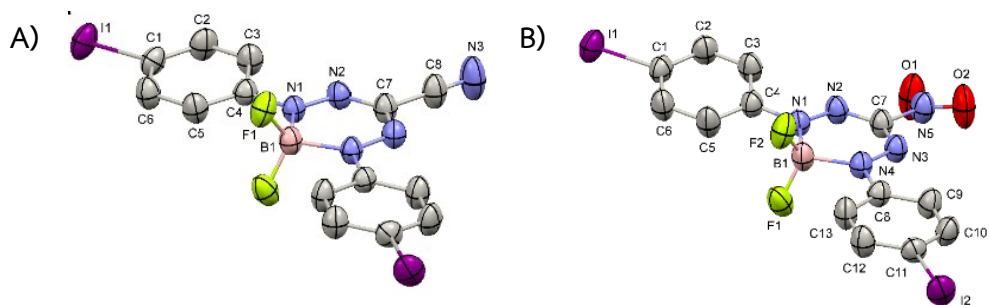


**Figure 4.20** Molecular structure of (A) BCI and (B) BNI, together with the atom-labeling scheme. The displacement ellipsoids are drawn at the 50% probability level. Selected bond lengths ( $\text{\AA}$ ): For (A)  $B1-N1 = 1.582(4)$ ,  $B1-F1 = 1.370(4)$ ,  $N1-N2 = 1.361(3)$ ,  $N2-C7 = 1.328(4)$ ; For (B)  $B1-N1 = 1.590(6)$ ,  $B1-N4 = 1.587(6)$ ,  $B1-F1 = 1.358(6)$ ,  $B1-F2 = 1.362(6)$ ,  $N1-N2 = 1.301(5)$ ,  $N3-N4 = 1.301(5)$ ,  $N2-C7 = 1.318(5)$ ,  $N3-C7 = 1.319(6)$ .

**Table 4.2** Crystal data and structure refinement details for two BF<sub>2</sub>-Formazanate complexes (BCI and BNI).

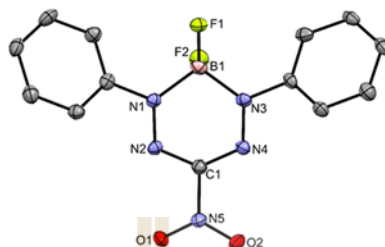
Crystallographic Data and Structural Refinement Details	BCI	BNI
Empirical formula	C <sub>14</sub> H <sub>8</sub> BF <sub>2</sub> I <sub>2</sub> N <sub>5</sub>	C <sub>13</sub> H <sub>8</sub> BF <sub>2</sub> I <sub>2</sub> N <sub>5</sub> O <sub>2</sub>
Formula weight	548.86	568.85
Temperature/K	298	298
Crystal system	monoclinic	triclinic
Space group	C2/c	P-1
a/Å	10.7846(9)	8.6783(8)
b/Å	14.9439(12)	9.5283(8)
c/Å	11.0187(14)	10.7544(9)
α/°	90	98.454(3)
β/°	110.824(3)	95.916(3)
γ/°	90	104.172(4)
Volume/Å <sup>3</sup>	1659.8(3)	843.83(13)
Z	4	2
ρ <sub>calc</sub> /cm <sup>3</sup>	2.196	2.239
μ/mm <sup>-1</sup>	30.019	29.647
F(000)	1024.0	532.0
Crystal size/mm <sup>3</sup>	0.25 × 0.2 × 0.13	0.3 × 0.2 × 0.16
Radiation	CuKα (λ = 1.54178)	CuKα (λ = 1.54178)
2θ range for data collection/°	10.586 to 144.834	8.4 to 145.456
Index ranges	-13 ≤ h ≤ 13, -18 ≤ k ≤ 18, -10 ≤ l ≤ 10	-11 ≤ h ≤ 11, -13 ≤ k ≤ 13, -13 ≤ l ≤ 13

**Table 4.2 (Continued)** Crystal data and structure refinement details for two  $\text{BF}_2^-$  Formazanate complexes (**BCI** and **BNI**).

Reflections collected	8294	22391
Independent reflections	1586 [R <sub>int</sub> = 0.0373, R <sub>sigma</sub> = 0.0290]	3329 [R <sub>int</sub> = 0.0496, R <sub>sigma</sub> = 0.0287]
Data/restraints/parameters	1586/0/111	3329/0/226
Goodness-of-fit on F <sup>2</sup>	1.102	1.096
Final R indexes [I >= 2σ (I)]	R <sub>1</sub> = 0.0281, wR <sub>2</sub> = 0.0836	R <sub>1</sub> = 0.0401, wR <sub>2</sub> = 0.1086
Final R indexes [all data]	R <sub>1</sub> = 0.0297, wR <sub>2</sub> = 0.0852	R <sub>1</sub> = 0.0434, wR <sub>2</sub> = 0.1120
Largest diff. peak/hole / e Å <sup>-3</sup>	0.67/-0.47	1.80/-0.36



**Table 4.3** The results of the Single-Crystal X-ray Diffraction Analysis for BF<sub>2</sub>-Formazanate Complexes **BCH**, **BNH**, **BCI** and **BNI**: It includes selected bond lengths (Å) with atom labels corresponding to the structure above the table.



Selected bond	BCH (Barbon et al., 2014)	BNH (Barbon et al., 2015)	BCI (This work)	BNI (This work)
N1–N2, N3–N4	1.290, 1.295	1.302, 1.304	1.297, 1.297	1.301, 1.302
C1–N2, C1–N4	1.341, 1.338	1.330, 1.318	1.328, 1.328	1.319, 1.318
N1–B1, N3–B1	1.575, 1.577	1.576, 1.563	1.581, 1.581	1.587, 1.590
N1–B1–N3	105.55	103.4	105.87	105.16
N2–N1–B1, N4– N3–B1	124.78, 124.32	121.5, 122.2	124.56, 124.56	124.65, 124.93
N2–C1–N4	129.33	130.00	130.29	131.70
C1–N2–N1, C1– N4–N3	117.14, 117.30	115.6, 115.5	117.35, 117.35	116.90, 116.46

#### 4.4 Electrochemical characterizations

The electrochemical properties of  $\text{BF}_2$ -Formazanate complexes were analyzed using cyclic voltammetry. As shown in Figure 4.21, **BCH** and **BNH** exhibited two distinct reversible reduction waves. The first reduction potential, ranging from -0.4 to -0.5 V, corresponds to a single-electron reduction process, resulting in the formation of radical anions for both compounds. The second reduction potential, observed between -1.5 and -1.67 V, represents another single-electron process, where the radical anions are converted into dianions (Buguis, Maar, Staroverov, and Gilroy, 2021). Interestingly, the redox potential waves showed minimal variation when the substituent at the 3-position was changed from cyano (-CN) to nitro (-NO<sub>2</sub>). The excellent electrochemical reversibility observed in these compounds is likely due to the stabilization of frontier molecular orbitals by the four nitrogen atoms in the backbone of the ring. These findings are consistent with previously reported results for  $\text{BF}_2$ -Formazanate complexes (Barbon et al., 2015).

Similarly, Figure 5B shows the cyclic voltammograms of the iodinated derivatives, **BCI** and **BNI** (Barbon et al., 2015). In contrast to **BCH** and **BNH**, both oxidation and reduction waves of **BCI** and **BNI** were electrochemically irreversible. This lack of reversibility is likely attributed to the influence of iodine atoms in the structure. For **BNI**, the irreversible oxidation potential was slightly higher (-0.5 V) than that of **BCI** (-0.6 V), which can be explained by the stronger electron-withdrawing effect of -NO<sub>2</sub> compared to -CN. The reduction potentials of both iodinated complexes were approximately -1.5 V, representing an irreversible redox process. These results emphasize that the incorporation of heavy atoms, such as iodine, plays a critical role in determining the electrochemical reversibility of these compounds.

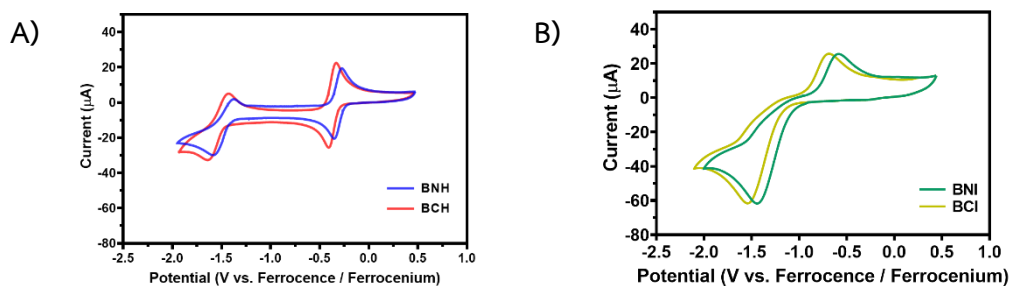


**Figure 4.21** Cyclic voltammograms of (A) non-iodinated complexes (BNH and BCH) and (B) iodinated complexes (BNI and BCI) recorded at  $100 \text{ mV s}^{-1}$  in 1 mM acetonitrile solutions containing 0.1 M tetrabutylammonium hexafluorophosphate as supporting electrolyte.

#### 4.5 Computational studies

Because the computational results on BCI and BNI are not significantly different, only the results on BCI are discussed in detail. The equilibrium structures of BCI and BNI obtained from the DFT/B3LYP/6-311G and TD-DFT/B3LYP/6-311G methods are shown in Figure 4.22A&B, respectively. In the gas phase (dielectric constant,  $\epsilon=1$ ), the equilibrium structures in the  $S_0$ ,  $S_1$ , and  $T_1$  states are characterized as bent, propeller, and perfect planar structures, respectively.

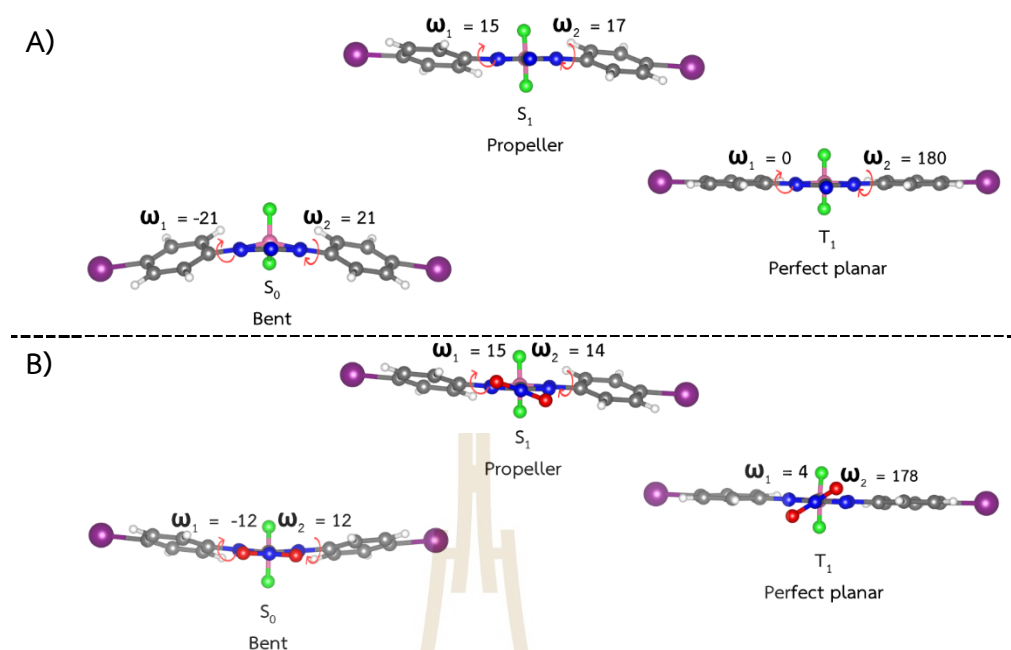


**Figure 4.22** The equilibrium structures of **(A) BCI** and **(B) BNI** in the  $S_0$ ,  $S_1$ , and  $T_1$  states in the gas phase ( $\epsilon = 1$ ). the torsional angle in degree represents  $\omega_1$  and  $\omega_2$ .

For **BCI**, The investigation of the HOMO and LUMO structures ( $\epsilon = 1$ ) in Figure 4.23A revealed that in the  $S_0$  state, the HOMO is characterized by the high electron density distribution on both phenyl rings (strong  $\pi$  character), whereas in the  $S_1$  and  $T_1$  states, the electron density redistribution occurs from the iodine atoms to the heterocyclic ring, leading to a decrease in the  $\pi$  character at the phenyl rings and an increase in the electron density at the nitrogen atoms of the heterocyclic framework. TD-DFT/B3LYP/6-311G calculations ( $\epsilon = 1$ ) suggest the vertical excitation energy,  $\Delta E_{\text{Ex}} = 2.42$  eV or  $\lambda_{\text{max}}^{\text{Cal}} = 513$  nm for **BCI** ( $\Delta E_{\text{Ex}} = 2.33$  eV or  $\lambda_{\text{max}}^{\text{Cal}} = 532$  nm for **BNI**). The UV-vis spectra obtained from the TD-DFT/B3LYP/6-311G method in Figure 4.24 show two characteristic peaks namely, in DMSO ( $\epsilon = 47$ ), the outstanding peak is at  $\lambda_{\text{max}}^{\text{Cal}} = 531$  nm and a small peak at  $\lambda_{\text{max}}^{\text{Cal}} = 427$  nm. These characteristic peaks are compared well with the UV-vis spectra obtained in the experiment, for which the main peak is at  $\lambda_{\text{max}}^{\text{Exp}} = 521$  nm and a shoulder at  $\lambda_{\text{max}}^{\text{Exp}} = 462$  nm.

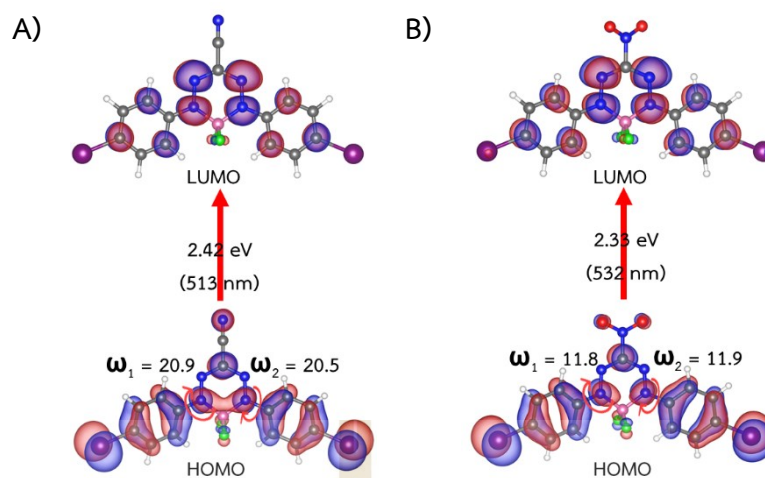


**Figure 4.23** HOMO and LUMO of the equilibrium structure of (A) BCI and (B) BNI in the  $S_0$  state ( $\epsilon = 1$ ). (isosurface: 0.025).

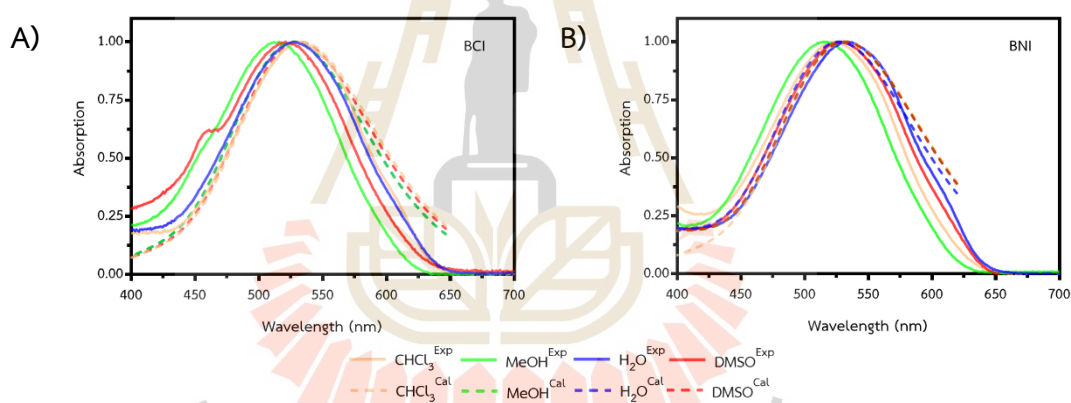


**Figure 4.24** UV-vis absorption spectra of  $BF_2$ -Formazanate complexes in various solvents obtained from theoretical and experimental methods.

The calculated photophysical properties in Table 4.4 show that solvent polarity does not strongly affect the absorption spectra; it is usual that the  $\lambda_{max}^{Cal}$  obtained from the TD-DFT/B3LYP/6-311G method are systematically red-shifted compared with the experimental values (approximately 6 nm for BCI and BNI).

It appears that the HOMO and LUMO are approximately the same in low and high local dielectric environments (Figure 4.25), whereas the  $S_0 \rightarrow S_1$  excitation energies ( $\Delta E^{Exp, Cal}$  in Table 4.4) increase with an increase in the solvent polarity.

A comparison of the spectroscopic results in different solvent polarities shows good agreement between the theoretical and experimental values. It should be noted that due to the higher electron-withdrawing ability of the nitro group in **BNI**, the  $\pi$  character of the HOMO at the heterocyclic framework is smaller than in **BCI**. This leads to a smaller vertical excitation energy for **BNI** compared with **BCI**,  $\Delta E^{\text{Ex,Cal}} = 2.33$  and 2.42 eV, respectively. In  $\text{CHCl}_3$  ( $\epsilon = 4.8$ ), (Myers, 2005) while the trend of the effect of the local dielectric environment is the same as that for **BCI**, the main peak of the UV-vis spectra is 24 nm red-shifted compared with **BNI**. To search for the intersections of the  $S_1$  and  $S_0$  and the  $S_1$  and  $T_1$  states, the potential energy curves for the rotations of  $\omega_1$  and  $\omega_2$  were computed in the  $S_1$  state using the NEB method;  $\omega_1$  and  $\omega_2$  were varied in the range of  $-20$ – $180$  degrees. Because the potential energy curves and reaction paths for **BCI** (Figures 4.26–4.28) and **BNI** (Figures 4.29–4.31) are virtually the same, only the results on **BCI** are discussed in detail.

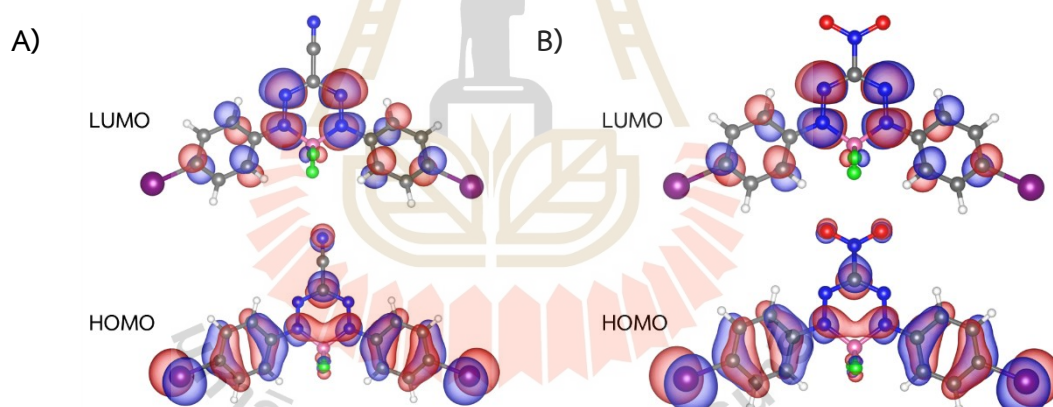
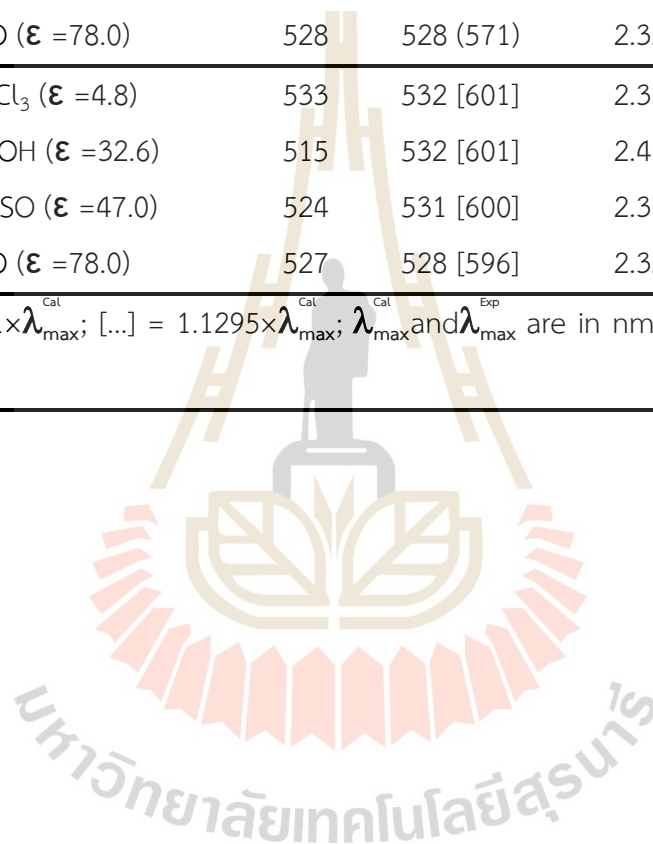


Figure 4.25 HOMO-LUMO of the equilibrium structures at ground state in COSMO of (A) **BCI** and (B) **BNI**. ( $\epsilon = 78$ , Isosurface: 0.025)

**Table 4.4** The calculated photophysical properties of BF<sub>2</sub>-Formazanate dyes in various solvents, using the equilibrium structures obtained from DFT/B3LYP/6-311G optimizations.

CDP	Conditions	$\lambda_{\max}^{\text{Exp}}$	$\lambda_{\max}^{\text{Cal}}$	$\Delta E^{\text{Ex,Exp}}$	$\Delta E^{\text{Ex,Cal}}$
BCI	CHCl <sub>3</sub> ( $\epsilon$ =4.8)	531	534 (577)	2.33	2.32 (2.15)
	MeOH ( $\epsilon$ =32.6)	516	528 (571)	2.40	2.34 (2.17)
	DMSO ( $\epsilon$ =47.0)	521	532 (575)	2.38	2.33 (2.16)
	H <sub>2</sub> O ( $\epsilon$ =78.0)	528	528 (571)	2.35	2.35 (2.17)
BNI	CHCl <sub>3</sub> ( $\epsilon$ =4.8)	533	532 [601]	2.33	2.33 [2.06]
	MeOH ( $\epsilon$ =32.6)	515	532 [601]	2.41	2.33 [2.06]
	DMSO ( $\epsilon$ =47.0)	524	531 [600]	2.37	2.33 [2.07]
	H <sub>2</sub> O ( $\epsilon$ =78.0)	527	528 [596]	2.35	2.35 [2.08]

(...) =  $1.0811 \times \lambda_{\max}^{\text{Cal}}$ ; [...] =  $1.1295 \times \lambda_{\max}^{\text{Cal}}$ ;  $\lambda_{\max}^{\text{Cal}}$  and  $\lambda_{\max}^{\text{Exp}}$  are in nm;  $\Delta E^{\text{Ex,Cal}}$  and  $\Delta E^{\text{Ex,Exp}}$  are in eV.



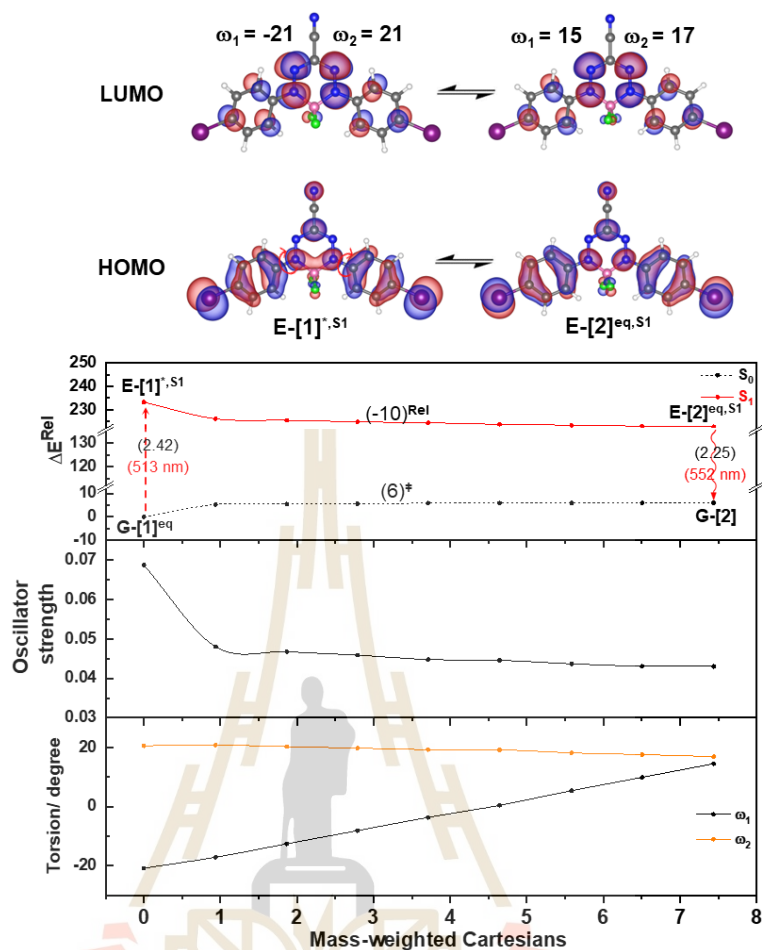


**Figure 4.26** The  $S_0$  and  $S_1$  potential energy curves for librational motions of both phenyl residues in BCI of  $E-[1]^*,S_1$  to  $E-[2]^{eq,S_1}$  obtained from the DFT/B3LYP/6-311G and TD-DFT/B3LYP/6-311G method, respectively. The solid line represents the NEB potential energies in  $S_1$  state, and the dashed line denotes the energies in the  $S_0$  state calculated using the geometries on NEB potential energy curves. Oscillator strength and torsional angles ( $\omega_1$  and  $\omega_2$ ) are in au and degree, respectively. Energies are in kJ/mol unless specified otherwise.  $\Delta E^{Rel}$  = relative energy with respect to the total energy of  $G-[1]^{eq}$ ;  $(...)^{Rel}$  = relative energy with respect to the transition structure;  $(...)^{\ddagger}$  = energy barrier;  $E-[...]^*$  =  $S_0 \rightarrow S_1$  vertically excited structure;  $E-[...]^{eq}$  = equilibrium structure in the excited state.

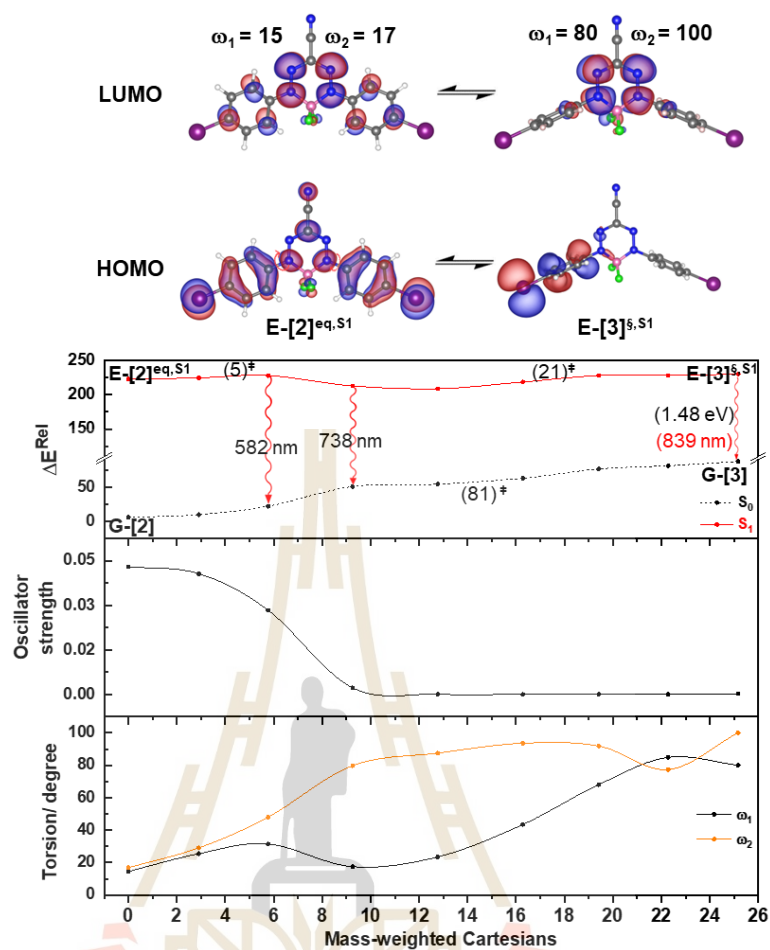


**Figure 4.27** The  $S_0$  and  $S_1$  potential energy curves for librational motions of both phenyl residues in BCI of  $E-[2]^{eq,S1}$  to  $E-[3]^{S,S1}$  obtained from the DFT/B3LYP/6-311G and TD-DFT/B3LYP/6-311G method, respectively. The solid line represents the NEB potential energies in  $S_1$  state, and the dashed line denotes the energies in the  $S_0$  state calculated using the geometries on NEB potential energy curves. Oscillator strength and torsional angles ( $\omega_1$  and  $\omega_2$ ) are in au and degree, respectively. Energies are in kJ/mol unless specified otherwise.  $\Delta E^{Rel}$  = relative energy with respect to the total energy of  $G-[1]^{eq}$ ;  $(...)^{Rel}$  = relative energy with respect to the transition structure;  $(...)^{\ddagger}$  = energy barrier;  $E-[...]^{eq}$  = equilibrium structure in the excited state;  $E-[...]^S$  = structure at the  $S_1/T_1$  intersection.

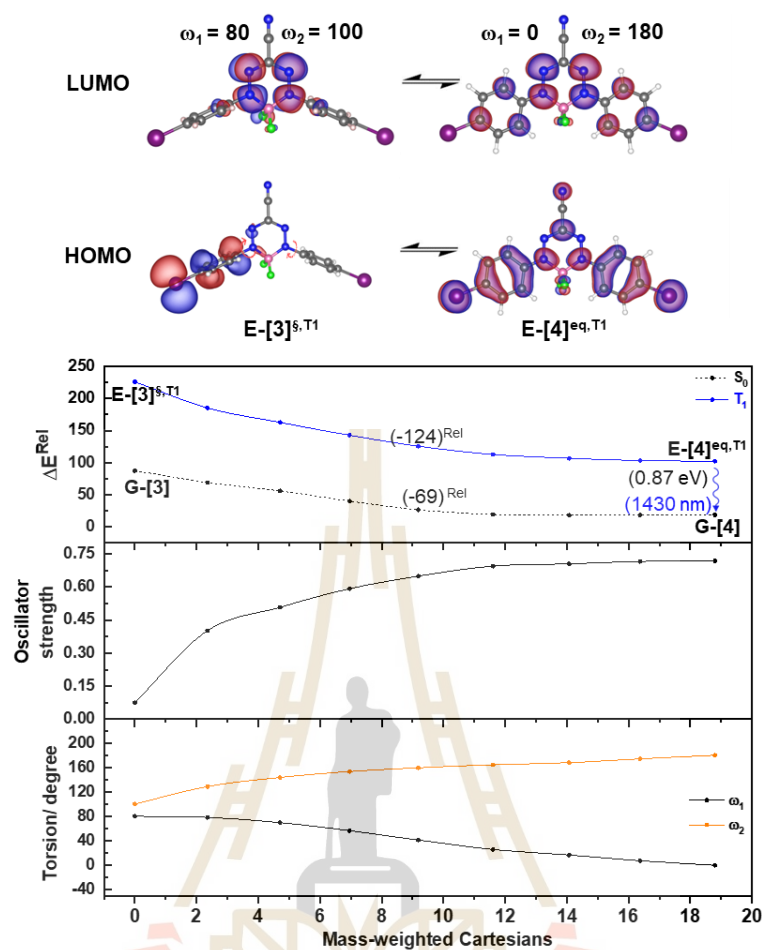


**Figure 4.28** The  $S_0$  and  $T_1$  potential energy curves for librational motions of both phenyl residues in BCI of  $E-[3]^{S,T1}$  to  $E-[4]^{eq,T1}$  obtained from the DFT/B3LYP/6-311G and TD-DFT/B3LYP/6-311G method, respectively. The solid line represents the NEB potential energies in  $T_1$  state, and the dashed line denotes the energies in the  $S_0$  state calculated using the geometries on NEB potential energy curves. Oscillator strength and torsional angles ( $\omega_1$  and  $\omega_2$ ) are in au and degree, respectively. Energies are in kJ/mol unless specified otherwise.  $\Delta E^{Rel}$  = relative energy with respect to the total energy of  $G-[1]^{eq}$ ;  $(...)^{Rel}$  = relative energy with respect to the transition structure;  $(...)^{\ddagger}$  = energy barrier;  $E-[...]^{eq}$  = equilibrium structure in the excited state;  $E-[...]^S$  = structure at the  $S_1/T_1$  intersection.

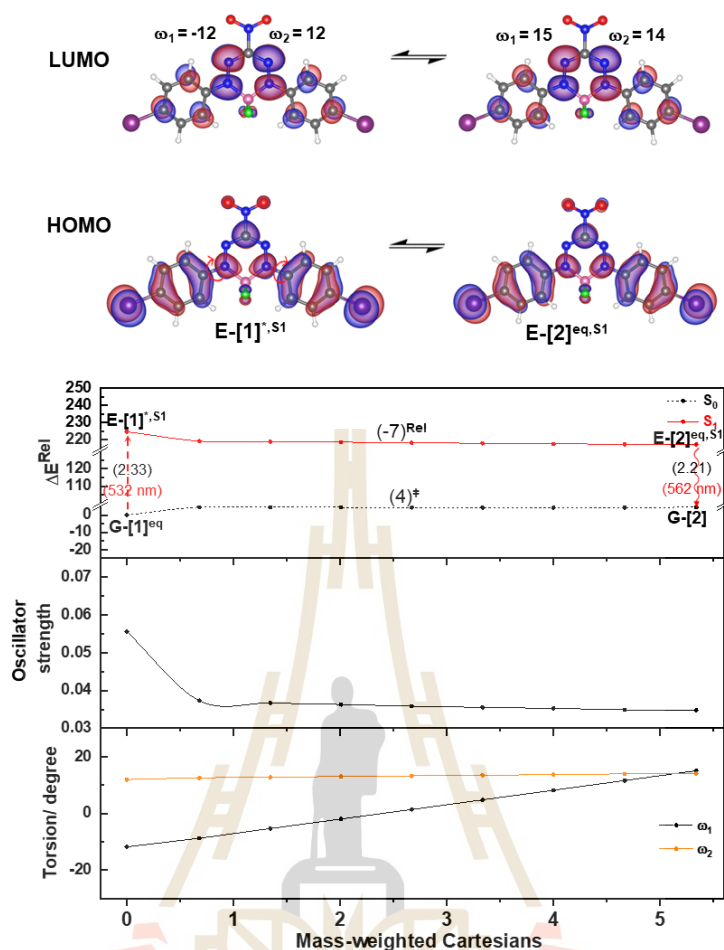


**Figure 4.29** The  $S_0$  and  $S_1$  potential energy curves for librational motions of both phenyl residues in BNI of  $E-[1]^{*,S1}$  to  $E-[2]^{eq,S1}$  obtained from the DFT/B3LYP/6-311G and TD-DFT/B3LYP/6-311G method, respectively. The solid line represents the NEB potential energies in  $S_1$  state, and the dashed line denotes the energies in the  $S_0$  state calculated using the geometries on NEB potential energy curves. Oscillator strength and torsional angles ( $\omega_1$  and  $\omega_2$ ) are in au and degree, respectively. Energies are in kJ/mol unless specified otherwise.  $\Delta E^{Rel}$  = relative energy with respect to the total energy of  $G-[1]^{eq}$ ;  $(...)^{Rel}$  = relative energy with respect to the transition structure;  $(...)^{\ddagger}$  = energy barrier;  $E-[...]^*$  =  $S_0 \rightarrow S_1$  vertically excited structure;  $E-[...]^{eq}$  = equilibrium structure in the excited state.

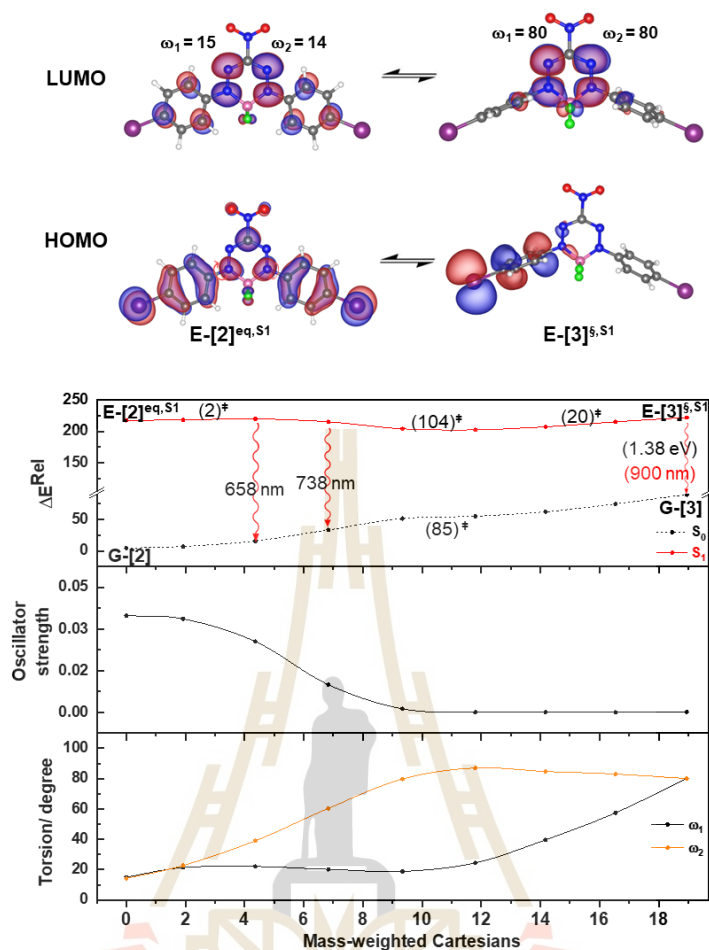


**Figure 4.30** The  $S_0$  and  $S_1$  potential energy curves for librational motions of both phenyl residues in BNI of  $E-[2]^{\text{eq},S_1}$  to  $E-[3]^{\text{S},S_1}$  obtained from the DFT/B3LYP/6-311G and TD-DFT/B3LYP/6-311G method, respectively. The solid line represents the NEB potential energies in  $S_1$  state, and the dashed line denotes the energies in the  $S_0$  state calculated using the geometries on NEB potential energy curves. Oscillator strength and torsional angles ( $\omega_1$  and  $\omega_2$ ) are in au and degree, respectively. Energies are in kJ/mol unless specified otherwise.  $\Delta E^{\text{Rel}}$  = relative energy with respect to the total energy of  $G-[1]^{\text{eq}}$ ;  $(\dots)^{\text{Rel}}$  = relative energy with respect to the transition structure;  $(\dots)^{\ddagger}$  = energy barrier;  $E-[...]^{\text{eq}}$  = equilibrium structure in the excited state;  $E-[...]^{\text{S}}$  = structure at the  $S_1/T_1$  intersection.

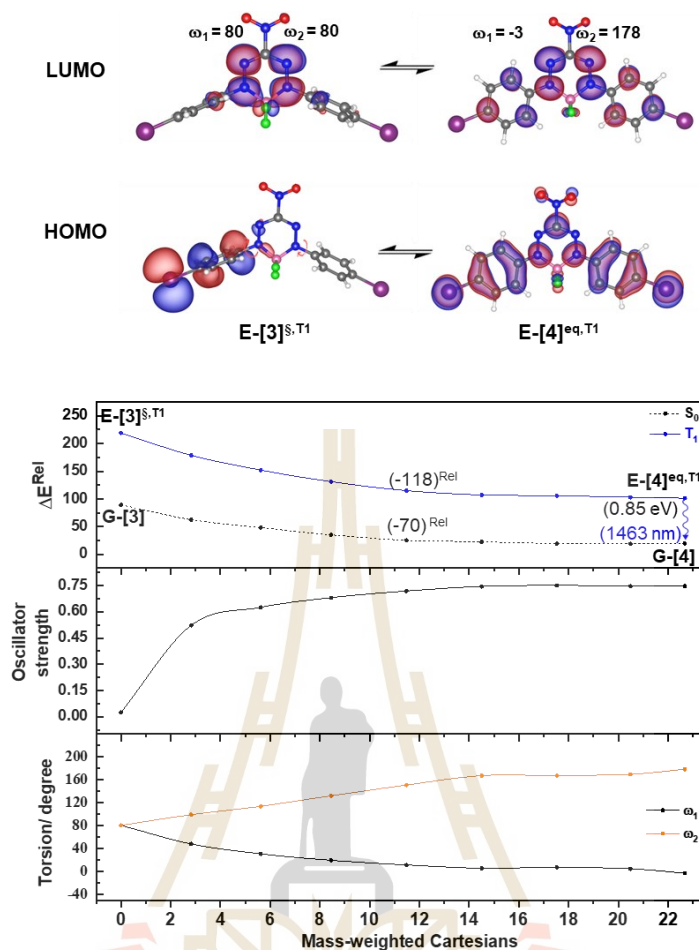


**Figure 4.31** The  $S_0$  and  $T_1$  potential energy curves for librational motions of both phenyl residues in BNI of E-[3]<sup>S,T1</sup> to E-[4]<sup>eq,T1</sup> obtained from the DFT/B3LYP/6-311G and TD-DFT/B3LYP/6-311G method, respectively. The solid line represents the NEB potential energies in  $T_1$  state, and the dashed line denotes the energies in the  $S_0$  state calculated using the geometries on NEB potential energy curves. Oscillator strength and torsional angles ( $\omega_1$  and  $\omega_2$ ) are in au and degree, respectively. Energies are in kJ/mol unless specified otherwise.  $\Delta E^{\text{Rel}}$  = relative energy with respect to the total energy of G-[1]<sup>eq</sup>; (...) <sup>Rel</sup> = relative energy with respect to the transition structure; (...) <sup>‡</sup> = energy barrier; E-[...] <sup>eq</sup> = equilibrium structure in the excited state; E-[...] <sup>S</sup> = structure at the  $S_1/T_1$  intersection.

The optimized reaction path for the photoluminescence of **BCI** (Figure 4.32) was obtained from the analysis of the potential energy curves (Figures 4.26–4.28 in supporting information). The results reveal that structure E-[2]<sup>eq,S1</sup> can be transformed into structure E-[3]<sup>S,S1</sup> with  $\Delta E^\ddagger = 0.07$  eV (8 kJ/mol) and a small energy gap between  $S_1$  and  $T_1$  states (the  $S_1/T_1$  intersection),  $\Delta E^{S_1 \rightarrow T_1} = -0.04$  eV (-4 kJ/mol). The possibility for the relaxation of structure E-[3]<sup>S,T1</sup> to the equilibrium structure in the  $T_1$  state was studied by performing the NEB calculations in the  $T_1$  state using structure E-[3]<sup>S,T1</sup> as the precursor and structure E-[4]<sup>eq,T1</sup> as the product. The result in Figure 4.32 shows a barrierless potential energy with the energy gap between the  $T_1$  and  $S_0$ ,  $\Delta E^{T_1 \rightarrow S_0} = 0.87$  eV (84 kJ/mol);  $\Delta E^{T_1 \rightarrow S_0}$  is close to the  ${}^3O_2 \rightarrow {}^1O_2$  reported in the literature to be  $\sim 0.97$  eV (94 kJ/mol) (Davies, 2003).

To confirm the heavy atom effect, the same calculations were conducted on **BCH** and **BNH** (the structures without iodine substituents). The results in Figures 4.34 and 4.35 show that the energy gaps at the  $T_1/S_1$  intersection ( $\Delta E^{S_1 \rightarrow T_1}$ ) of **BCH** and **BNH** were calculated as 0.30 eV (29 kJ/mol) and 0.14 eV (14 kJ/mol), respectively which are significantly larger than those of **BCI** and **BNI**, implying that ISC occurs more preferentially in **BCI** and **BNI**.

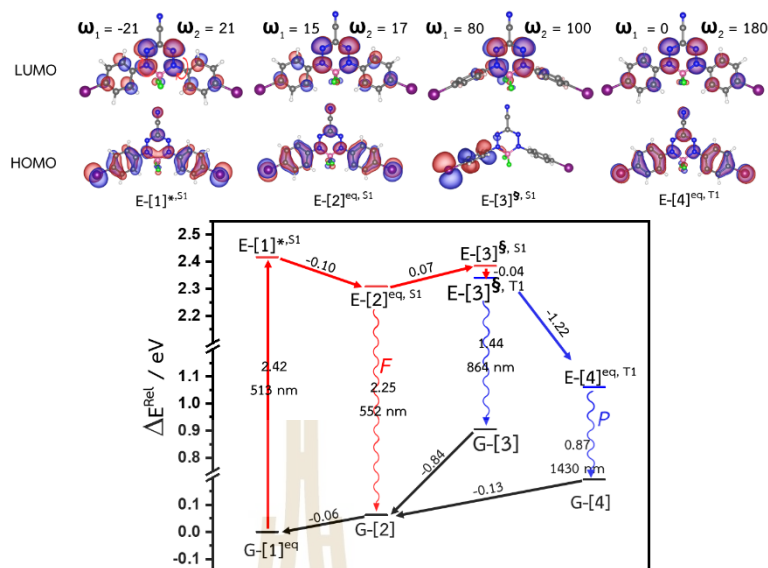


**Figure 4.32** The proposed mechanisms for excitation and radiation of BCI. The excitation energies are in eV. G = structure in the  $S_0$  state;  $E^{S1}$  and  $E^{T1}$  = structures in the  $S_1$  and  $T_1$  states;  $[...]^{eq}$  = equilibrium structure;  $[...]^S$  = structure at the  $S_1/T_1$  intersection.

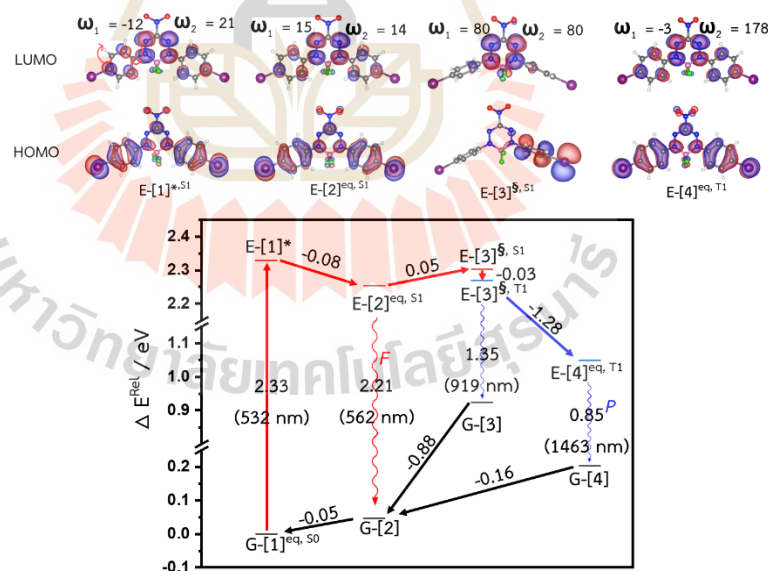


**Figure 4.33** The proposed mechanisms for excitation and radiation of BNI. The excitation energies are in eV. G = structure in the  $S_0$  state;  $E^{S1}$  and  $E^{T1}$  = structures in the  $S_1$  and  $T_1$  states;  $[...]^{eq}$  = equilibrium structure;  $[...]^S$  = structure at the  $S_1/T_1$  intersection.

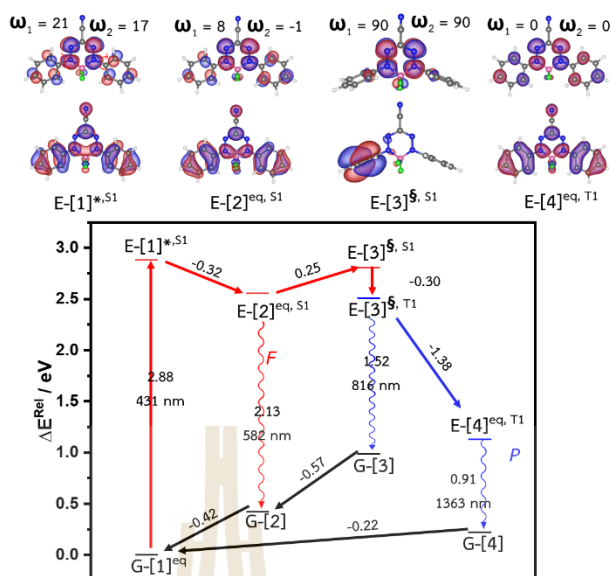


**Figure 4.34** The proposed mechanisms for excitation and radiation of BCH. The excitation energies are in eV. G = structure in the  $S_0$  state;  $E^{S1}$  and  $E^{T1}$  = structures in the  $S_1$  and  $T_1$  states;  $[...]^{eq}$  = equilibrium structure;  $[...]^s$  = structure at the  $S_1/T_1$  intersection.

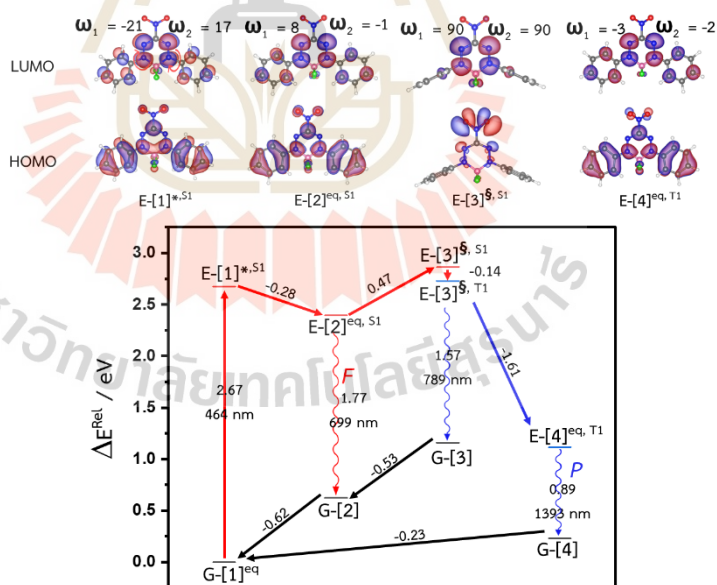


**Figure 4.35** The proposed mechanisms for excitation and radiation of BNH. The excitation energies are in eV. G = structure in the  $S_0$  state;  $E^{S1}$  and  $E^{T1}$  = structures in the  $S_1$  and  $T_1$  states;  $[...]^{eq}$  = equilibrium structure;  $[...]^s$  = structure at the  $S_1/T_1$  intersection.

## 4.6 Biological applications

To confirm the ability of **BCI** and **BNI** in PDT, a series of *in vitro* experiments were performed. The human liver hepatocellular carcinoma cells (HepG2) were used as a model in this study. First, the complexes were tested for their cytotoxicity in the absence and presence of activated light. As shown in Figures 4.36A and 4.36B, the cell viability reduced dramatically in a dose-dependent manner after the cells were treated with **BCI** (Figure 4.36A) and **BNI** (Figure 4.36B) followed by light irradiation at 532 nm for 15 min. The half-maximal inhibitory concentration ( $IC_{50}$ ) of both complexes is shown in Table 4.5 and Figure 4.36C and 4.36D. As the light dose increased, the lower  $IC_{50}$  could be achieved, which **BNI** seemed to be more effective than **BCI**.

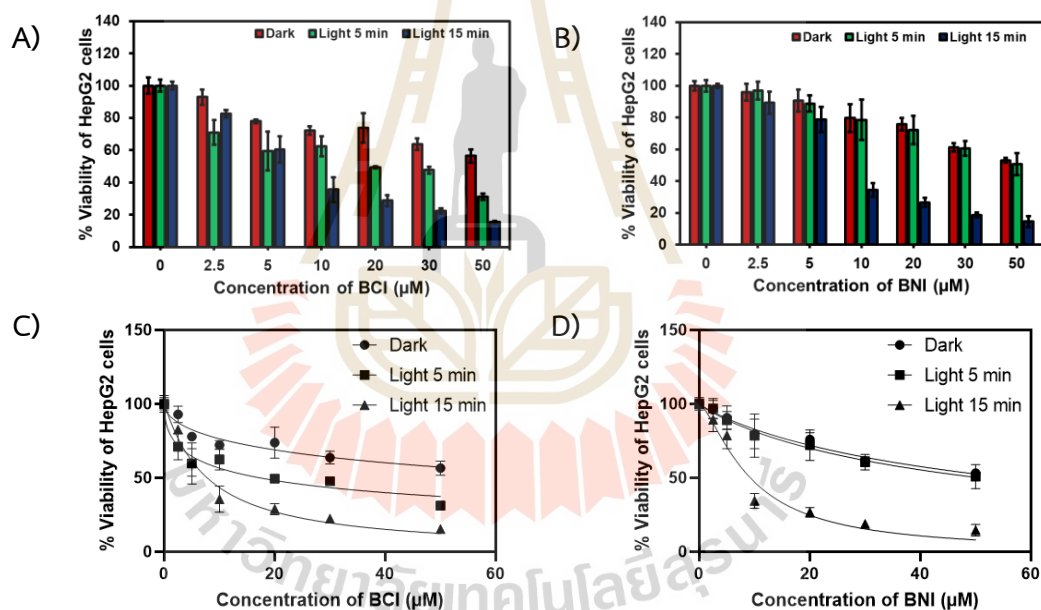


**Figure 4.36** The relative cell viability of HepG2 cells under irradiation (0, 5, or 15 min) after incubation with (A) **BCI** or (B) **BNI** (0-50 μM) for 24 h. Data are presented as means  $\pm$ SD (n=3), \*P <0.05, \*\*P <0.01, or \*\*\*P <0.001 are based on Student's T-test. The  $IC_{50}$  curves of (C) **BCI** and (D) **BNI** (0-50 μM) treated on HepG2 cells followed by light irradiation (0, 5, or 15 min).

**Table 4.5** The half maximal inhibitory concentration ( $IC_{50}$ ) of **BCI** and **BNI** under various conditions.

Conditions	$IC_{50}$ ( $\mu M$ )	
	BCI	BNI
Dark	>50	>50
Light 5 min	28.09	22.34
Light 15 min	10.52	6.17

The live/dead viability/cytotoxicity and intracellular singlet oxygen detection assays were carried out to further demonstrate that the cancer cells were eliminated by  $^1O_2$  generated from light activation. To distinguish between living and dead cells, propidium iodide (PI) and calcein AM were utilized. While PI can only enter dead cells through ruptured cell membranes, calcein AM can enter living cells and emit green fluorescence after being cleaved by intracellular esterase. As shown in Figures 4.37A&B, only cells that were exposed to **BCI** and **BNI**, particularly at high doses, followed by light irradiation exhibited discernible red fluorescence, indicating the light-triggered cell death in the presence of our probes. In contrast, the green fluorescence of the control cells (no light irradiation), cells exposed to irradiation without the compounds, cells incubated with the complexes (without light), and the cells treated with non-iodinated analogs (**BNH** and **BCH**) followed by light irradiation showed that they were largely still viable, with little to no red fluorescence (Figure 4.38).

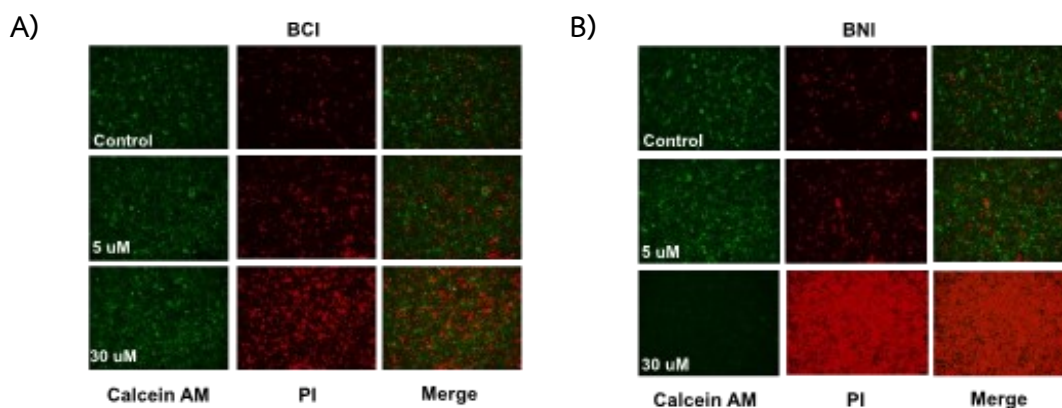


**Figure 4.37** The fluorescent images of LIVE/DEAD co-staining assay of HepG2 cells after treatment with (A) BCI and (B) BNI (5 or 30  $\mu\text{M}$ ) for 24 h then irradiation with light (15 min).

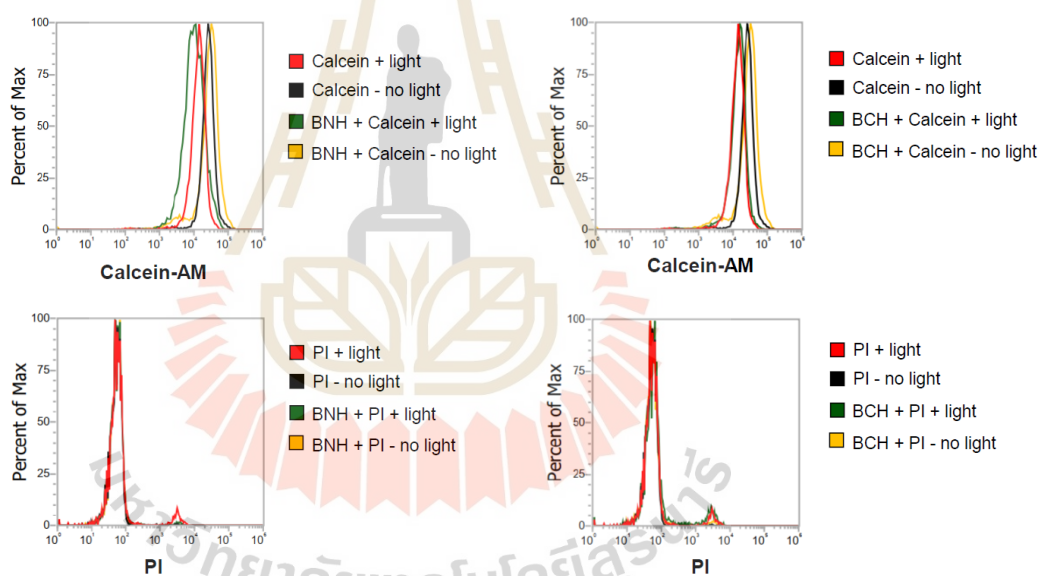


**Figure 4.38** The flow cytometry analysis of cells treated with BCH or BNH for 24 h, then stained with Calcein AM and PI compared with controls (cells no BCH or BNH treatment).

Additionally, to detect intracellular reactive oxygen species (ROS), 2',7'-dichlorofluorescein diacetate (DCFH-DA), a nonfluorescent compound, was used because it can be oxidized by ROS to create 2',7'-dichlorofluorescein (DCF), which exhibits green fluorescence inside living cells. As shown in Figure 4.38, intense green DCF fluorescence is detected only in HepG2 cells that have been treated with **BNI** before being exposed to light, implying that the ROS was created within the cells. No ROS were detected in the controls after irradiation (cells only, cells with DCFH-DA, and cells with **BNI**). Furthermore, a probe known as singlet oxygen sensor green (SOSG) was employed to detect  $^1\text{O}_2$  production within the cells (Gollmer et al., 2011). Cells exposed to **BCI** or **BNI** followed by light irradiation showed green fluorescence, which was not seen in the other control groups (Figure 4.39). As a result, it was concluded that while **BNI** can produce ROS, including  $^1\text{O}_2$ , **BCI** only produces  $^1\text{O}_2$  to destroy cancer cells.

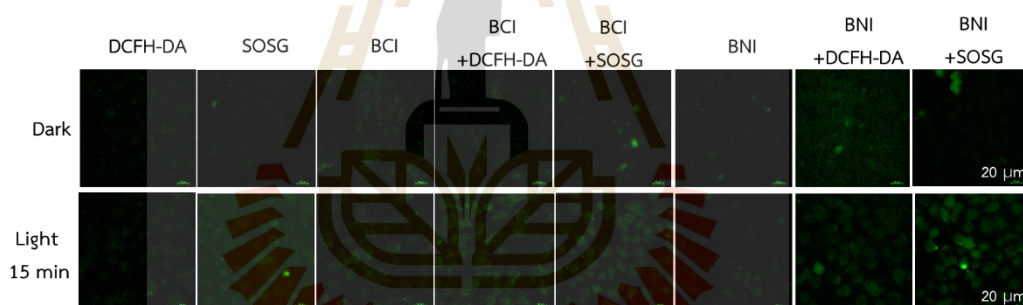


**Figure 4.39** The intracellular ROS and  $^1\text{O}_2$  detection in HepG2 cells using DCFH-DA and SOSG, respectively, after incubating the cells with **BCI** or **BNI** (10  $\mu\text{M}$ ) for 24 h followed by light illumination in comparison with dark conditions. Scale bars = 20  $\mu\text{m}$ .

In addition, we utilized flow cytometry to examine the PDT-assisted apoptosis of cancer cells induced by our iodine-containing  $\text{BF}_2$ -Formazanate complexes. To identify apoptotic cells, a kit containing Annexin V, fluorescein isothiocyanate (FITC), and PI were utilized.

When cells were in the early stages of apoptosis, phosphatidylserine was translocated from the inner face of the plasma membrane to the cell surface, where it interacted with Annexin V-FITC to produce green fluorescence (van Engeland, Nieland, Ramaekers, Schutte, and Reutelingsperger, 1998), (the population of cells shown at the top left of the diagram). Because PI is bound to the DNA within the dead cells, a red fluorescence was generated (the cell population shown on the bottom right of the diagram). During the final stages of apoptosis, the integrity of the cell membrane was compromised, allowing Annexin V and PI to enter the cells (the cell population shown in the top right of the diagram). Figure 4.40 demonstrates that cells treated with **BCI** and **BNI** and then exposed to light undergo early apoptosis at rates of 38 and 37%, respectively. In contrast, 12 and 51% of the cells treated with **BCI** and **BNI** and then exposed to light underwent late apoptosis, respectively. As anticipated, **BCH**-and **BNH**-treated cells did not undergo late apoptosis (Figure 4.41). Consequently, it is evident that the **BCI** and **BNI** induced post-PDT cell apoptosis, especially in the late stage, as demonstrated by the increased cell population in late apoptosis as measured by FACS in comparison to cells treated without light illumination.



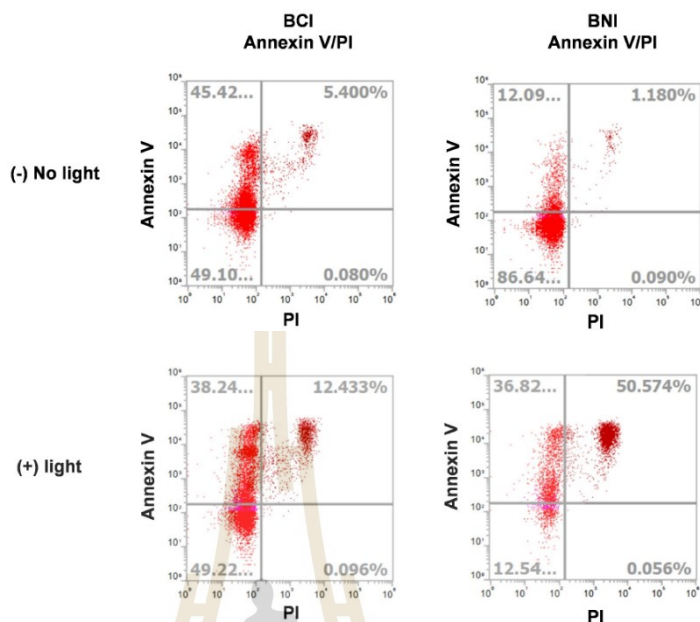


**Figure 4.40** The flow cytometry Annexin V fluorescein isothiocyanate (FITC)/propidium iodide (PI) apoptosis analysis of cells incubated with BCI and BNI (10  $\mu$ M) for 24 h.

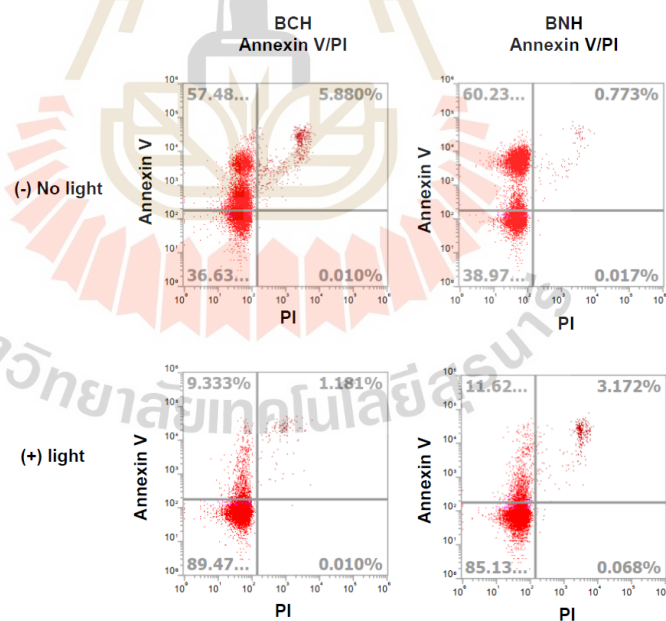
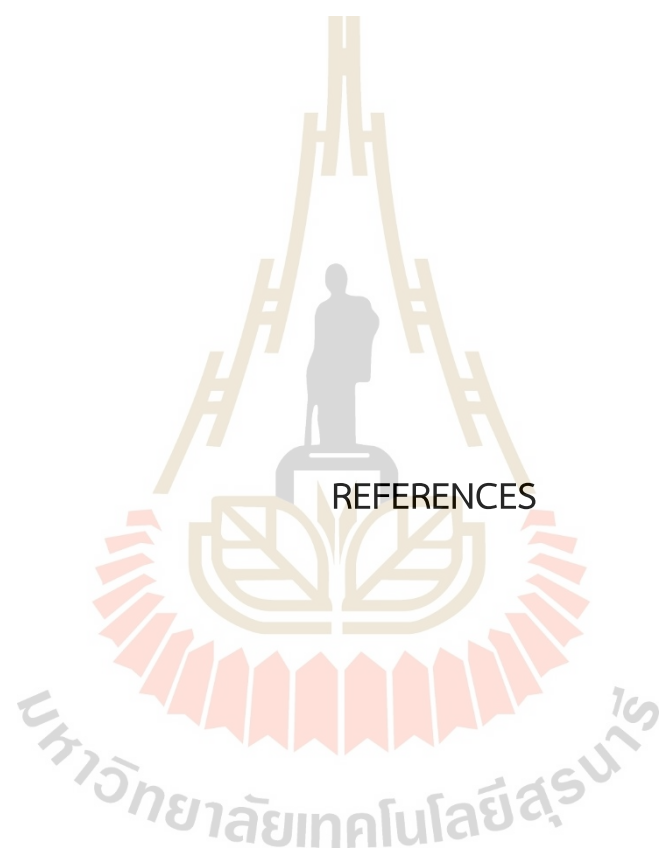


**Figure 4.41** The flow cytometry Annexin V fluorescein isothiocyanate (FITC)/propidium iodide (PI) apoptosis analysis of cells incubated with BCH and BNH (10  $\mu$ M) for 24 h.

## CHAPTER V

### CONCLUSION

The iodinated BF<sub>2</sub>-Formazanate complexes, **BCI** and **BNI**, were successfully synthesized and thoroughly analyzed. Their structures and purity were validated through NMR spectroscopy and X-ray crystallography. Absorption and fluorescence studies revealed red-shifted absorption in toluene and large Stokes shifts, highlighting their potential for bioimaging applications. Compared to the non-iodinated analogs (**BCH** and **BNH**), **BCI** and **BNI** displayed greater, bathochromic shifted absorption and emission, as well as notable singlet oxygen generation, making them promise for photodynamic therapy (PDT). In vitro experiments on HepG2 cells demonstrated their light dose-dependent cytotoxicity, with **BNI** outperforming **BCI** by producing both ROS and <sup>1</sup>O<sub>2</sub>, while **BCI** generated only <sup>1</sup>O<sub>2</sub>. Computational studies (DFT/B3LYP/6-311G and TD-DFT/B3LYP/6-311G) revealed minimal differences in the equilibrium structures of **BCI** and **BNI** across S<sub>0</sub>, S<sub>1</sub>, and T<sub>1</sub> states, and theoretical UV-vis spectra matched experimental data. Reaction path analysis indicated that phenyl ring rotations drive the S<sub>1</sub>/T<sub>1</sub> intersection and T<sub>1</sub>→S<sub>0</sub> phosphorescence. ISC was confirmed to occur more efficiently in **BCI** and **BNI** than in **BCH** and **BNH** due to favorable S<sub>1</sub> and T<sub>1</sub> energy gaps. Based on experimental and computational findings, mechanisms for fluorescence and phosphorescence were proposed, and **BCI** and **BNI** were identified as strong PDT candidates. However, further modifications are needed to improve their clinical potential, such as enhanced ROS production, longer wavelength emissions, and tumor-targeting capabilities with reduced dark toxicity.



REFERENCES

## REFERENCES

- Aryamueang, S., Chansaenpak, K., Hiranmartsuwan, P., Prommin, C., Suthirakun, S., Pinyou, P., . . . Kamkaew, A. (2022). Near-infrared aza-BODIPYs bearing tetraphenylethylene: Synthesis, photophysical studies, and cell imaging application. *Journal of Photochemistry and Photobiology A: Chemistry*, *433*, 114128. doi:<https://doi.org/10.1016/j.jphotochem.2022.114128>
- Balamurugan, S. G., Chen, G. P., Coriani, S., Diedenhofen, M., Frank, M. S., Franzke, Y. J., . . . Yu, J. M. (2020). TURBOMOLE: Modular program suite for ab initio quantum-chemical and condensed-matter simulations. *The Journal of Chemical Physics*, *152*(18). doi:[10.1063/5.0004635](https://doi.org/10.1063/5.0004635)
- Bao, G., Deng, R., Jin, D., and Liu, X. (2025). Hidden triplet states at hybrid organic–inorganic interfaces. *Nature Reviews Materials*, *10*(1), 28–43. doi:[10.1038/s41578-024-00704-y](https://doi.org/10.1038/s41578-024-00704-y)
- Barbon, S. M., Reinkeluers, P. A., Price, J. T., Staroverov, V. N., and Gilroy, J. B. (2014). Structurally Tunable 3-Cyanoformazanate Boron Difluoride Dyes. *Chemistry – A European Journal*, *20*(36), 11340–11344. doi:<https://doi.org/10.1002/chem.201404297>
- Barbon, S. M., Staroverov, V. N., and Gilroy, J. B. (2015). Effect of Extended  $\pi$  Conjugation on the Spectroscopic and Electrochemical Properties of Boron Difluoride Formazanate Complexes. *The Journal of Organic Chemistry*, *80*(10), 5226–5235. doi:[10.1021/acs.joc.5b00620](https://doi.org/10.1021/acs.joc.5b00620)
- Buguis, F. L., Maar, R. R., Staroverov, V. N., and Gilroy, J. B. (2021). Near-Infrared Boron Difluoride Formazanate Dyes. *Chemistry – A European Journal*, *27*(8), 2854–2860. doi:<https://doi.org/10.1002/chem.202004793>
- Chen, H., Liu, L., Qian, K., Liu, H., Wang, Z., Gao, F., . . . Cheng, Z. (2022). Bioinspired large Stokes shift small molecular dyes for biomedical fluorescence imaging. *Science Advances*, *8*(32), eabo3289. doi:[doi:10.1126/sciadv.abo3289](https://doi.org/10.1126/sciadv.abo3289)

- Davies, M. J. (2003). Singlet oxygen-mediated damage to proteins and its consequences. *Biochemical and Biophysical Research Communications*, 305(3), 761-770. doi:[https://doi.org/10.1016/S0006-291X\(03\)00817-9](https://doi.org/10.1016/S0006-291X(03)00817-9)
- DeRosa, M. C., and Crutchley, R. J. (2002). Photosensitized singlet oxygen and its applications. *Coordination Chemistry Reviews*, 233-234, 351-371. doi:[https://doi.org/10.1016/S0010-8545\(02\)00034-6](https://doi.org/10.1016/S0010-8545(02)00034-6)
- Dolomanov, O. V., Bourhis, L. J., Gildea, R. J., Howard, J. A., and Puschmann, H. (2009). OLEX2: a complete structure solution, refinement and analysis program. *Journal of applied crystallography*, 42(2), 339-341.
- Galland, M., Le Bahers, T., Banyasz, A., Lascoux, N., Duperray, A., Grichine, A., . . . Maury, O. (2019). A “Multi-Heavy-Atom” Approach toward Biphotonic Photosensitizers with Improved Singlet-Oxygen Generation Properties. *Chemistry – A European Journal*, 25(38), 9026-9034. doi:<https://doi.org/10.1002/chem.201901047>
- Gandra, N., Frank, A. T., Le Gendre, O., Sawwan, N., Aebisher, D., Liebman, J. F., . . . Gao, R. (2006). Possible singlet oxygen generation from the photolysis of indigo dyes in methanol, DMSO, water, and ionic liquid, 1-butyl-3-methylimidazolium tetrafluoroborate. *Tetrahedron*, 62(46), 10771-10776.
- Gilroy, J. B., and Otten, E. (2020). Formazanate coordination compounds: synthesis, reactivity, and applications. *Chemical Society Reviews*, 49(1), 85-113. doi:[10.1039/C9CS00676A](https://doi.org/10.1039/C9CS00676A)
- Gollmer, A., Arnbjerg, J., Blaikie, F. H., Pedersen, B. W., Breitenbach, T., Daasbjerg, K., . . . Ogilby, P. R. (2011). Singlet Oxygen Sensor Green®: Photochemical Behavior in Solution and in a Mammalian Cell. *Photochemistry and Photobiology*, 87(3), 671-679. doi:<https://doi.org/10.1111/j.1751-1097.2011.00900.x>
- Hak, A., Ravasaheb Shinde, V., and Rengan, A. K. (2021). A review of advanced nanoformulations in phototherapy for cancer therapeutics. *Photodiagnosis and Photodynamic Therapy*, 33, 102205. doi:<https://doi.org/10.1016/j.pdpdt.2021.102205>

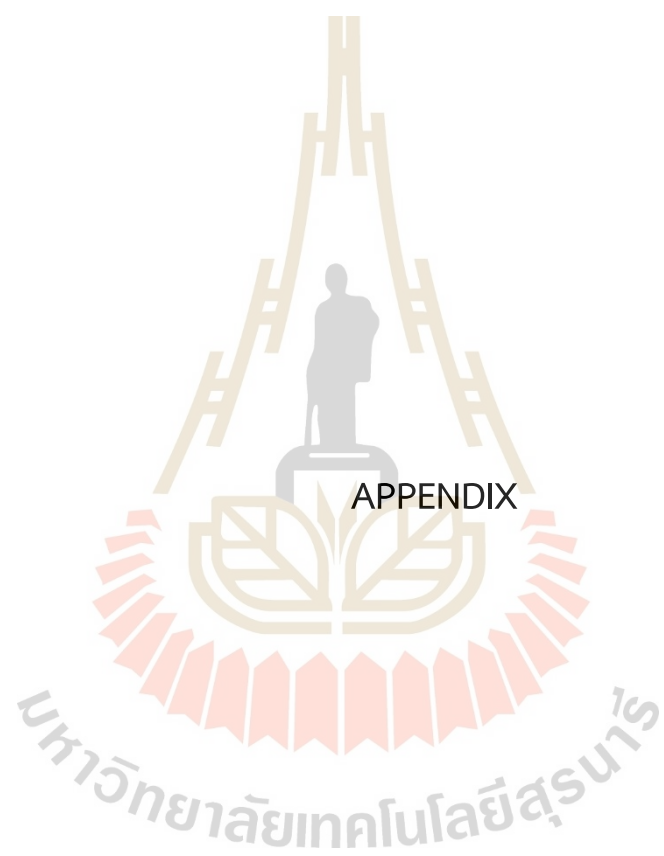
- Hamzehpoor, E., Ruchlin, C., Tao, Y., Liu, C.-H., Titi, H. M., and Perepichka, D. F. (2023). Efficient room-temperature phosphorescence of covalent organic frameworks through covalent halogen doping. *Nature Chemistry*, *15*(1), 83-90. doi:10.1038/s41557-022-01070-4
- Hiranmartsuwan, P., Ma, X., Nootem, J., Daengngern, R., Kamkaew, A., Pinyou, P., . . . Chansaenpak, K. (2022). Synthesis and properties of AIE-active Triazaborolopyridiniums toward fluorescent nanoparticles for cellular imaging and their biodistribution in vivo and ex vivo. *Materials Today Chemistry*, *26*, 101121. doi:https://doi.org/10.1016/j.mtchem.2022.101121
- Hu, W., Zhang, X.-F., and Liu, M. (2021). Thioetherification Inducing Efficient Excited Triplet State and Singlet Oxygen Generation: Heavy Atom-Free BODIPY Photosensitizer Based on the  $S_1(n, \pi^*)$  State. *The Journal of Physical Chemistry C*, *125*(9), 5233-5242. doi:10.1021/acs.jpcc.1c00001
- Kamkaew, A., Lim, S. H., Lee, H. B., Kiew, L. V., Chung, L. Y., and Burgess, K. (2013). BODIPY dyes in photodynamic therapy. *Chemical Society Reviews*, *42*(1), 77-88. doi:10.1039/C2CS35216H
- Kästner, J., Carr, J. M., Keal, T. W., Thiel, W., Wander, A., and Sherwood, P. (2009). DL-FIND: An Open-Source Geometry Optimizer for Atomistic Simulations. *The Journal of Physical Chemistry A*, *113*(43), 11856-11865. doi:10.1021/jp9028968
- Kumar, A., Kołaski, M., Lee, H. M., and Kim, K. S. (2008). Photoexcitation and Photoionization Dynamics of Water Photolysis. *The Journal of Physical Chemistry A*, *112*(24), 5502-5508. doi:10.1021/jp711485b
- Li, H., Kamasah, A., Matsika, S., and Suits, A. G. (2019). Intersystem crossing in the exit channel. *Nature Chemistry*, *11*(2), 123-128. doi:10.1038/s41557-018-0186-5
- Lipunova, G. N., Fedorchenko, T. G., and Chupakhin, O. N. (2019). New Aspects of the Chemistry of Formazans. *Russian Journal of General Chemistry*, *89*(6), 1225-1245. doi:10.1134/S1070363219060203
- Loudet, A., and Burgess, K. (2007). BODIPY dyes and their derivatives: syntheses and spectroscopic properties. *Chemical reviews*, *107*(11), 4891-4932.

- Maar, R. R., Barbon, S. M., Sharma, N., Groom, H., Luyt, L. G., and Gilroy, J. B. (2015). Evaluation of Anisole-Substituted Boron Difluoride Formazanate Complexes for Fluorescence Cell Imaging. *Chemistry – A European Journal*, *21*(44), 15589-15599. doi:<https://doi.org/10.1002/chem.201502821>
- Macrae, C. F., Edgington, P. R., McCabe, P., Pidcock, E., Shields, G. P., Taylor, R., . . . van de Streek, J. (2006). Mercury: visualization and analysis of crystal structures. *Journal of applied crystallography*, *39*(3), 453-457. doi:[doi:10.1107/S002188980600731X](https://doi.org/10.1107/S002188980600731X)
- Metz, S., Kästner, J., Sokol, A. A., Keal, T. W., and Sherwood, P. (2014). ChemShell—a modular software package for QM/MM simulations. *WIREs Computational Molecular Science*, *4*(2), 101-110. doi:<https://doi.org/10.1002/wcms.1163>
- Miao, X., Hu, W., He, T., Tao, H., Wang, Q., Chen, R., . . . Huang, W. (2019). Deciphering the intersystem crossing in near-infrared BODIPY photosensitizers for highly efficient photodynamic therapy. *Chemical Science*, *10*(10), 3096-3102. doi:[10.1039/C8SC04840A](https://doi.org/10.1039/C8SC04840A)
- Myers, D. B. J. (2005). Common Solvents Used in Organic Chemistry: Table of Properties. *ACS Division of Organic Chemistry*. Retrieved from <https://organicchemistrydata.org/solvents/>
- Nootem, J., Sattayanon, C., Daengngern, R., Kamkaew, A., Wattanathana, W., Wannapaiboon, S., . . . Chansaenpak, K. (2021). BODIPY-pyridylhydrazone probe for fluorescence turn-on detection of Fe<sup>3+</sup> and its bioimaging application. *Chemosensors*, *9*(7), 165.
- Nootem, J., Sattayanon, C., Namuangruk, S., Rashatasakhon, P., Wattanathana, W., Tumcharern, G., and Chansaenpak, K. (2020). Solvatochromic triazaborolopyridinium probes toward ultra-sensitive trace water detection in organic solvents. *Dyes and Pigments*, *181*, 108554. doi:<https://doi.org/10.1016/j.dyepig.2020.108554>

- Pham, T. C., Nguyen, V.-N., Choi, Y., Lee, S., and Yoon, J. (2021). Recent Strategies to Develop Innovative Photosensitizers for Enhanced Photodynamic Therapy. *Chemical reviews*, *121*(21), 13454-13619. doi:10.1021/acs.chemrev.1c00381
- Piskorz, J., Porolnik, W., Kucinska, M., Dlugaszewska, J., Murias, M., and Mielcarek, J. (2021). BODIPY-Based Photosensitizers as Potential Anticancer and Antibacterial Agents: Role of the Positive Charge and the Heavy Atom Effect. *ChemMedChem*, *16*(2), 399-411. doi:https://doi.org/10.1002/cmdc.202000529
- Recio, P., Alessandrini, S., Vanuzzo, G., Pannacci, G., Baggioli, A., Marchione, D., . . . Barone, V. (2022). Intersystem crossing in the entrance channel of the reaction of O(3P) with pyridine. *Nature Chemistry*, *14*(12), 1405-1412. doi:10.1038/s41557-022-01047-3
- Redmond, R. W., and Gamlin, J. N. (1999). A Compilation of Singlet Oxygen Yields from Biologically Relevant Molecules. *Photochemistry and Photobiology*, *70*(4), 391-475. doi:https://doi.org/10.1111/j.1751-1097.1999.tb08240.x
- SAINT Version 8.34A 2013; Bruker AXS: Madison, W., USA. (2013).
- Sednev, M. V., Belov, V. N., and Hell, S. W. (2015). Fluorescent dyes with large Stokes shifts for super-resolution optical microscopy of biological objects: a review. *Methods and applications in fluorescence*, *3*(4), 042004.
- Sharma, N., Barbon, S. M., Lalonde, T., Maar, R. R., Milne, M., Gilroy, J. B., and Luyt, L. G. (2020). The development of peptide-boron difluoride formazanate conjugates as fluorescence imaging agents. *RSC Advances*, *10*(32), 18970-18977.
- Sheldrick, G. M. (1996). Program for empirical absorption correction of area detector data. *Sadabs*.
- Sheldrick, G. M. (2015a). Crystal structure refinement with SHELXL. *Acta Crystallographica Section C: Structural Chemistry*, *71*(1), 3-8.
- Sheldrick, G. M. (2015b). SHELXT-Integrated space-group and crystal-structure determination. *Acta Crystallographica Section A: Foundations and Advances*, *71*(1), 3-8.

- Sholl, D. S., and Steckel, J. A. (2009). Density Functional Theory—A Practical Introduction. *Wiley, Hoboken*.
- Siriwibool, S., Kaekratoke, N., Chansaenpak, K., Siwawannapong, K., Panajapo, P., Sagarik, K., . . . Kamkaew, A. (2020). Near-Infrared Fluorescent pH Responsive Probe for Targeted Photodynamic Cancer Therapy. *Scientific Reports*, *10*(1), 1283. doi:10.1038/s41598-020-58239-5
- Siriwibool, S., Wangngae, S., Chansaenpak, K., Wet-osot, S., Lai, R.-Y., Noisa, P., . . . Kamkaew, A. (2022). Indomethacin-based near-infrared photosensitizer for targeted photodynamic cancer therapy. *Bioorganic Chemistry*, *122*, 105758. doi:https://doi.org/10.1016/j.bioorg.2022.105758
- van Engeland, M., Nieland, L. J. W., Ramaekers, F. C. S., Schutte, B., and Reutelingsperger, C. P. M. (1998). Annexin V-Affinity assay: A review on an apoptosis detection system based on phosphatidylserine exposure. *Cytometry*, *31*(1), 1-9. doi:https://doi.org/10.1002/(SICI)1097-0320(19980101)31:1<1::AID-CYTO1>3.0.CO;2-R
- Wang, C., and Qian, Y. (2019). A novel BODIPY-based photosensitizer with pH-active singlet oxygen generation for photodynamic therapy in lysosomes. *Organic and Biomolecular Chemistry*, *17*(34), 8001-8007. doi:10.1039/C9OB01242G
- Wang, S., Zhang, C., Fang, F., Fan, Y., Yang, J., and Zhang, J. (2023). Beyond traditional light: NIR-II light-activated photosensitizers for cancer therapy. *Journal of Materials Chemistry B*, *11*(35), 8315-8326. doi:10.1039/D3TB00668A
- Wang, X., Shi, H., Ma, H., Ye, W., Song, L., Zan, J., . . . Huang, W. (2021). Organic phosphors with bright triplet excitons for efficient X-ray-excited luminescence. *Nature Photonics*, *15*(3), 187-192. doi:10.1038/s41566-020-00744-0
- Xiao, Y.-F., Chen, J.-X., Chen, W.-C., Zheng, X., Cao, C., Tan, J., . . . Lee, C.-S. (2021). Achieving high singlet-oxygen generation by applying the heavy-atom effect to thermally activated delayed fluorescent materials. *Chemical Communications*, *57*(40), 4902-4905. doi:10.1039/D0CC08323B

- Yan, Z.-A., Lin, X., Sun, S., Ma, X., and Tian, H. (2021). Activating Room-Temperature Phosphorescence of Organic Luminophores via External Heavy-Atom Effect and Rigidity of Ionic Polymer Matrix. *Angewandte Chemie International Edition*, 60(36), 19735-19739. doi:<https://doi.org/10.1002/anie.202108025>
- Zhang, Y., Yang, Z., Zheng, X., Yang, L., Song, N., Zhang, L., . . . Xie, Z. (2020). Heavy atom substituted near-infrared BODIPY nanoparticles for photodynamic therapy. *Dyes and Pigments*, 178, 108348. doi:<https://doi.org/10.1016/j.dyepig.2020.108348>
- Zhao, W., Wang, L., Zhang, M., Liu, Z., Wu, C., Pan, X., . . . Quan, G. (2024). Photodynamic therapy for cancer: mechanisms, photosensitizers, nanocarriers, and clinical studies. *MedComm*, 5(7), e603. doi:<https://doi.org/10.1002/mco2.603>
- Zou, J., Wang, P., Wang, Y., Liu, G., Zhang, Y., Zhang, Q., . . . Dong, X. (2019). Penetration depth tunable BODIPY derivatives for pH triggered enhanced photothermal/photodynamic synergistic therapy. *Chemical Science*, 10(1), 268-276. doi:[10.1039/C8SC02443J](https://doi.org/10.1039/C8SC02443J)
- Zou, J., Yin, Z., Ding, K., Tang, Q., Li, J., Si, W., . . . Dong, X. (2017). BODIPY Derivatives for Photodynamic Therapy: Influence of Configuration versus Heavy Atom Effect. *ACS Applied Materials and Interfaces*, 9(38), 32475-32481. doi:[10.1021/acsami.7b07569](https://doi.org/10.1021/acsami.7b07569)

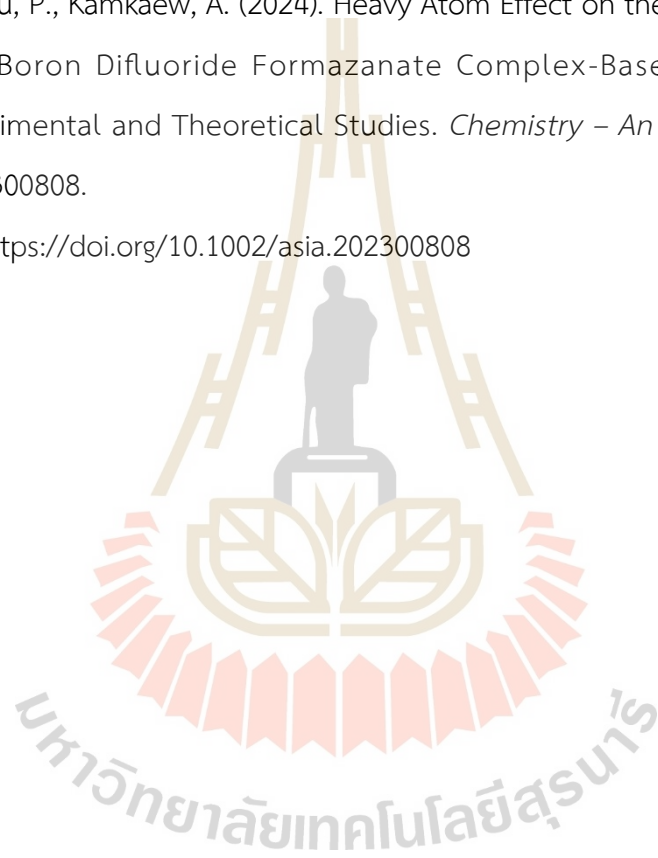


APPENDIX

APPENDIX  
THESIS OUTPUT

Khrootkaew, T., Wangngae, S., Chansaenpak, K., Rueantong, K., Wattanathana, W., Pinyou, P., Kamkaew, A. (2024). Heavy Atom Effect on the Intersystem Crossing of a Boron Difluoride Formazanate Complex-Based Photosensitizer: Experimental and Theoretical Studies. *Chemistry – An Asian Journal*, 19(1), e202300808.

doi:<https://doi.org/10.1002/asia.202300808>



## CURRICULUM VITAE

**Name:** Tunyawat Khrootkaew

**Date of Birth:** October 26<sup>th</sup>, 1999 at Surin, Thailand

### Education:

- 2022 - present      M.Sc. in Chemistry (International Program), Suranaree University of Technology, Thailand (expected 2025).
- 2018 - 2021      B.Sc. in Chemistry, Suranaree University of Technology, Thailand. (First-class honors)

### Internship:

- Visiting scholar at Texas A&M University, Texas, USA for 6 months, which was under the supervision of Prof. Dr. Kevin Burgess.

### Scholarships:

- Development and Promotion of Science and Technology Talents project (DSPT), supported by the Thai government (2021 – present).
- Academic Excellence scholarships, supported by Suranaree University of Technology (2018-2020).

### Conferences and presentations:

- 9<sup>th</sup> EuChemS Chemistry Congress (ECC9 2024).
- Science Postgrad Annual Research Conference 2023 (SPARC 2023)
- Pure and Applied Chemistry International Conference 2023 (PACCON2023).
- DSPT Conference Science and Technology 2022.

### Awards:

- 2022 1<sup>st</sup> Best oral presentation award at DSPT conference science and technology.